Review

Nanoframes as a Resilient Candidate for the Solution of Broader Spectra of Catalysis Challenges

Fawad Ahmad *, Qurat ul Ain , Shafaq Zahid , Takashiro Akitsu *

Posted Date: 31 January 2024

doi: 10.20944/preprints202401.2198.v1

Keywords: nanoframes, catalysis,; syntesis, applications

Review

Nanoframes as a Resilient Candidate for the Solution of Broader Spectra of Catalysis Challenges

Fawad Ahmad [1,*], Qurat ul Ain [1], Shafaq Zahid1 and Takashrio Aktisu [2,*]

[1] Department of Chemistry, University of Wah, Quaid Avenue, Wah Cantt., (47010), Punjab and Pakistan
[2] Department of Chemistry, Faculty of Science, Tokyo University of Science, Tokyo, Japan
* Correspondence: fawad.ahmad@uow.edu.pk (F.A.); akitsu2@rs.tus.ac.jp (T.A.)

Abstract: Metal nanoframes have gained tremendous attention in the domain of modern research and development due to their distinctive 3D spatial structure, efficient physiochemical properties, and comparatively good activity. Different strategies have been implicated by the researchers to design nano frame of varying chemical nature and shapes. Most of the synthetic protocols being adopted to design anano framee, mainly consist of two main steps, nucleation and growth of solid particles and secondly excavation of the interiors. In this context, many synthetic methods are overviewed. To show their unprecedented performance or activity, a few applications in catalytic, biomedical, theranostic, SERS, sensing of different materials, reduction of CO_2, etc are also discussed.

Keywords: nanoframes; catalysis,; syntesis; applications

1. Introduction

Different nanostructures have been synthesized previously by many research groups which include nanostars [1,2],nanobowls [3],nanorings [4],nanohexagons [5], nanopeapods [6],nanowalls [7],nanotubes [8], nanowires [9],nanorods [10]. Various vacant nanostructures have been synthesized ie nanobox [11–13] nanocages [14–16], nanoshells [17–19],nanoframes. [20,21]. Among all of these nanomaterials, hollow structures have acquired a lot of heed just because of their distinctive physical, chemical, catalytic, magnetic, electronic, and optical characteristics as compared to their bulk material. [22,23]. Among all of the above-discussed vacant nanomaterials, the appreciable open structure is possessed by nanoframes. They are defined as nanocrystals that only consist of ridges lacking faces. Nanoframes of different shapes are reported in literature i-e cubic, octahedral, dodecahedral, icosahedral, and plasmonic tripod, [24–28]. Various synthetic strategies have been used to synthesize nanoframes. Whatever synthetic protocol is being followed, it generally involves two main steps [23]. Initially, nucleation and growth of primary particles take place and then excavation of interiors happens [29,30]. In addition to the most commonly used synthetic strategies like galvanic replacement reaction, one-pot synthesis, and etching, some other methods have also been used by the researcher i-e thermal reductions, template-assisted synthesis [31], self-assembly of nanoparticles [32], solvothermal methods [33,34]. Metallic nanoframes have a distinctive morphology which makes them most suitable for their use in the catalytic domain. [35–37]. While referring to the stability of these metal nanoframe-like structures in comparison to other heterogenous catalysts, the former is the most stable one. The reason is that a high surface area to volume ratio in the latter is achieved by decreasing the catalyst size which in turn threatens their stability. However, in the former case excavation of material from the interior of the catalyst takes place which in turn creates greater room for the catalytic reaction to proceed. Apart from their efficient catalytic activity in ORR, EOR, MOR, HER, and biomass upgrading, many efforts have been made to use them in other domains as well. Their shape, size and composition can be customize [38] according to the demand.

In this review, different synthetic strategies for nanoframes are discussed including GRR(galvanic replacement reaction), one-pot synthesis, oxidative etching, photocatalytic template-

 doi:10.20944/preprints202401.2198.v1

assisted method, solvothermal technique, self-assembly of nanoparticles, thermal reductions, de-alloying of alloy nanocrystal, edge selected deposition of different metals on the template, face selected carving of the solid nanocrystal. Various nanoframes like metal NFs, alloy metal NFs, and doped metal NFs are also discussed. To elaborate efficiency of nanoframes many applications are described too including biomedical, theranostic, SERS, carbon dioxide reduction, sensing of different gaseous materials like VOCs, hydrogen sulfide gas, detection of cobalt ions, detection of dyes, electrochemical production of hydrogen peroxide in acids, suitable lithium-ion battery anode material.

2. Synthetic Approaches

2.1. Face Selected Carving of Solid Nanocrystals

This method includes selective dissolution of solid nanocrystal faces to synthesize Nano frames [39]. The monometallic nanocrystals exhibit surface inhomogeneity due to different factors like crystallographic defects, grain boundary, vacancy, dislocation, etc. octahedral nanocrystal is converted into octahedral nanoframe by using this method (Figure 1A) However, it is not always the case that the nanoframe formed has the same thickness at all the edges. This problem can be resolved by the use of a reducing agent during the chemical reaction to supplement the carving process with deposition. [40].The reducing agent should have profound reduction power so that by tuning the rate of deposition and rate of etching, one can control the thickness of edges. In the case of bimetallic nanocrystals, if one metal at the faces has low reduction potential and the other metal at the vertices and edges has high reduction potential then the one at the faces will be easily dissolute by etching agent and the one at the edges will remain there (Figure 1B) Due to the difference in diffusing rate between two metallic species in an alloy (Kirkendall effect) [41], rhombic dodecahedron can be synthesized.

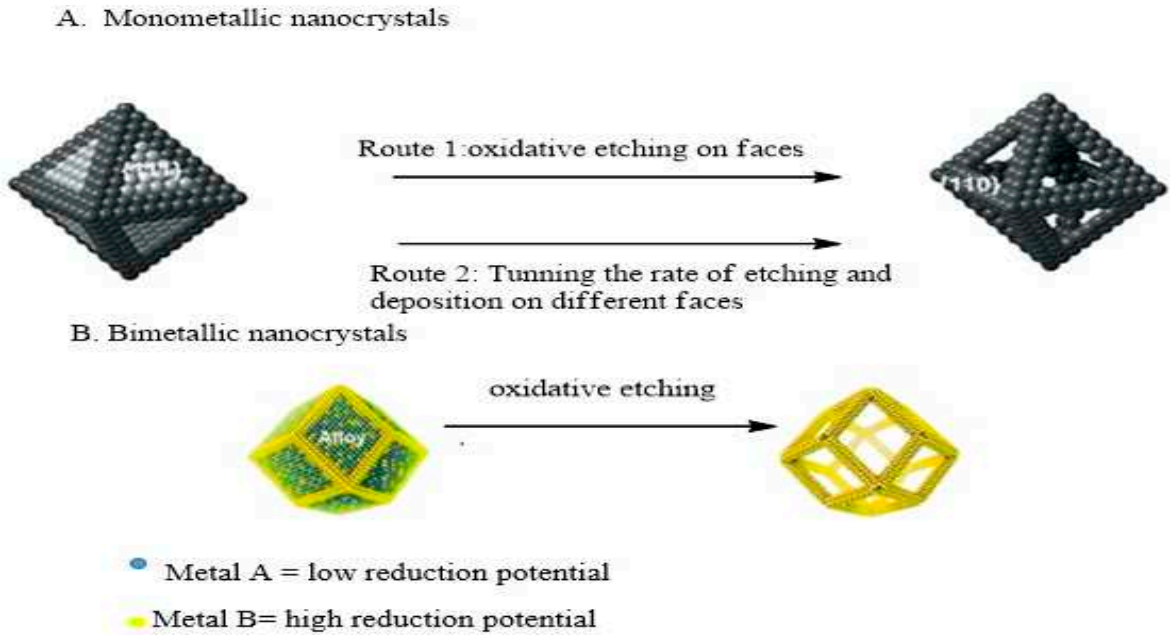

Figure 1. General schematic digram to show synthesis of nanoframes from monometallic octahedron (A) and bimetallic dodecahedron nanocrystal (B) based upon carving of atoms from side faces.

In the case of bimetallic nanocrystals, Pt-Ni nanoframe have been synthesized from Pt-Ni nanocrystals through the phase segregation method at the nanoscale [42]. The chemicals used for nanocrystal preparation were Pt (acetylacetonate)$_2$, Ni(acetylacetonate)$_2$, steric acid, octadecylamine(ODA), CO. The reaction conditions maintained were 1atm, 170^{0}C. CO was performing the dual function of surface stabilizer and reducing agent. After 1h, Pt –Ni core-shell

 doi:10.20944/preprints202401.2198.v1

octahedral nanocrystal was formed, and after 5 h the concentration of Pt at the edges of the octahedral increased due to the diffusion of Pt atoms. Afterward this octahedral was immersed in acetic acid at 100^{0}C for 1 hour to remove preferably Ni component and Pt-Ni nanoframe was synthesized. A generalized overview to synthesize Pt-Ni nanoframe using the aforementioned synthetic protocol can be taken from (Figure 2). TEM images are shown in Figure 3(A-D). No doubt it is a remarkable synthetic method for nanoframe synthesis. However, understanding its mechanism is ambiguous as it offers no information regarding intermediate species.

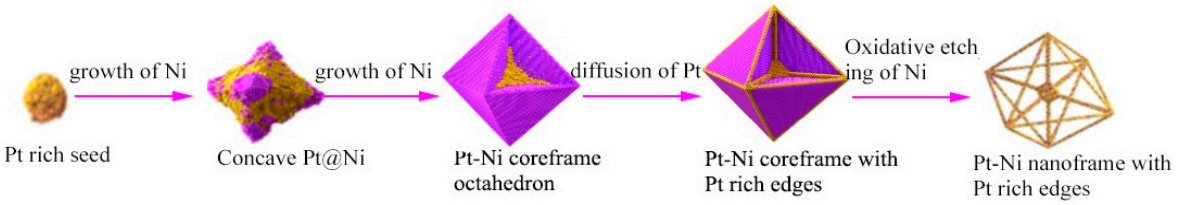

Figure 2. Schematic representation to design Pt-Ni nanoframe with Pt-rich edges.

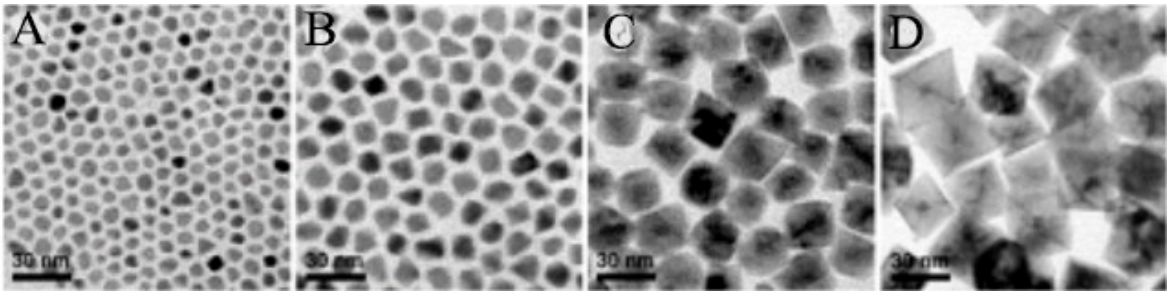

Figure 3. TEM images obtained at different points during the synthesis of Pt-Ni nanoframe showing shape changings during the whole procedure.

2.2. Edge Selected Deposition of Different Metals on Template

For cubic nanocrystals, the surface energy is more as compared to vertices and edges as the faces are made least active by the use of a capping agent [43] so instead of using an approach of direct carving of atoms from nanocrystals, we can do a deposition of another metal on edges and vertices of the nanocrystal. The second metal is selectively deposited at the edges and vertices. Eventually, the core is then removed either by oxidative etching [44] or by galvanic replacement reaction. depicts the formation of a cubic nanoframe when metal B (deposited) is more reactive than metal A [45]. After the etching of metal A from the core, the resultant nanoframe formed will only contain metal B at vertices and edges as shown in (Figure 4).

Despite it being a spectacular synthetic technique to synthesize nanoframe with clear morphology, there exists inter-diffusion between the atoms of the core and frame during the deposition or etching process [46]. Consequently, more undesired elements will be there in the end product.

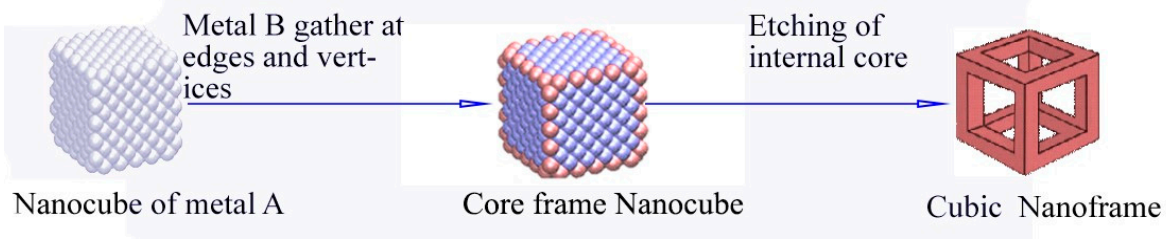

Figure 4. Schematic diagram depicting the formation of nanoframe made up of metal B by selective deposition on vertices and edges of nanocube made of metal A followed by etching.

 doi:10.20944/preprints202401.2198.v1

2.3. De-Alloying of Hollow Alloy Nanocrystals

In this method, galvanic replacement is initiated between metal A and metal B at the faces of the nanocube to generate pinholes in it. [47] After that metal, A is continuously carved and a hollow nanostructure will be formed. Finally, a Nano box will be obtained with walls made up of A-B alloy and free of pores. Now dealloying of metal A will take place using a chemical etchant and the Nano box will convert into nanoframe made up of pure metal B as shown in (Figure 5)

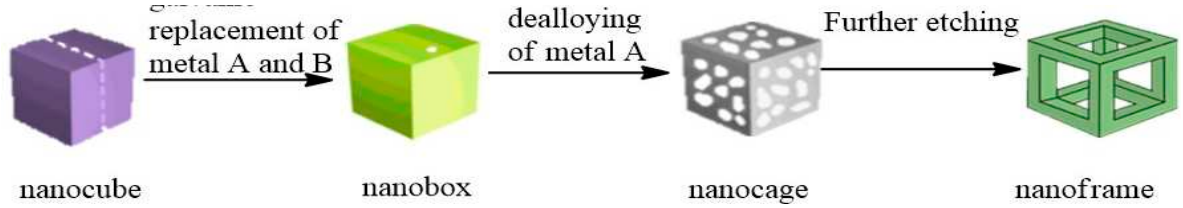

Figure 5. Schematic representation for the formation first of A-B alloy and then cubic nanoframe of metal B by dealloying of metal A from A-B nano box using a chemical etchant.

2.4. Nanoframe-Directed Deposition

In this synthetic approach, nanoframe will act as a template, and deposition of other metals takes place on it and hence augmenting the mechanical strength of nanoframe. [48]. It depends upon the growth mode that either the deposited metal will create a complete shell on the nanoframe or it would be randomly distributed on the nanoframe. [49]. The ratio between the rate of deposition and rate of surface diffusion of the atoms present on the surface is responsible for maintaining the final morphology of the nanoframe. When the rate of diffusion is greater than the rate of deposition $R_{diffusion} > R_{deposition}$ it is said to be conformal growth and vice versa ($R_{diffusion} < R_{deposition}$ would be called as island growth as shown in (Figure 6)

This strategy can be used to deposit useful materials onto the surface of the nanoframe. [50]. However, this approach has not been practically applied due to certain limitations i-e less quantity of nanoframe formed and their structural delicacy.

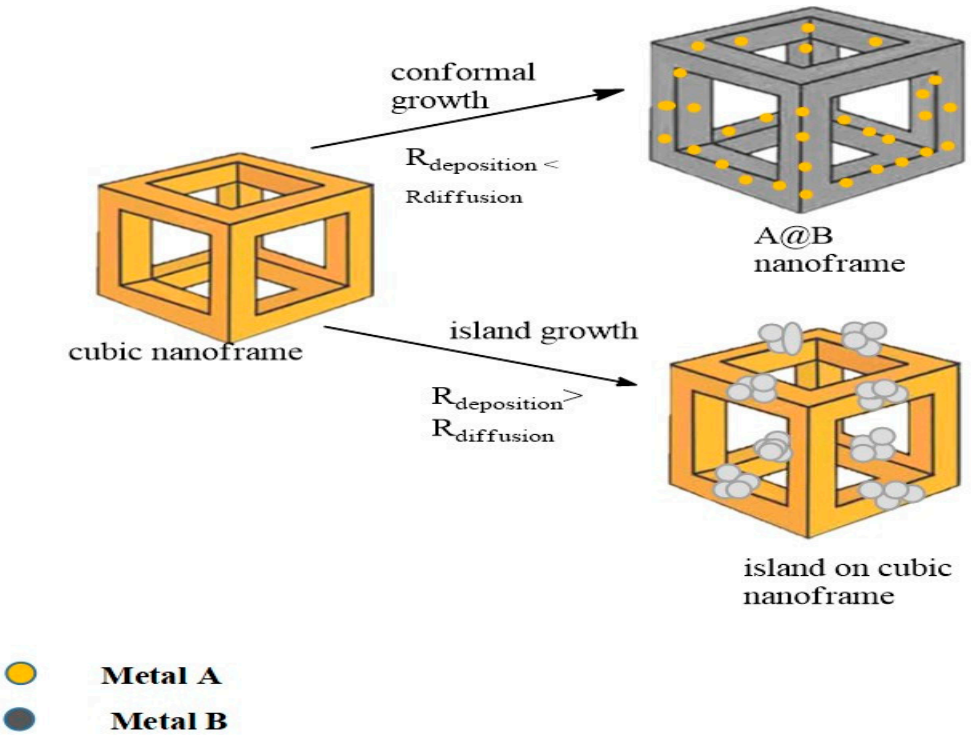

Figure 6. Scheme showing how growth rate effect either the deposited metal evolve into a complete shell on the nanoframe ridges or randomly distributed to form discrete islands or spikes on it.

 doi:10.20944/preprints202401.2198.v1

2.5. One-Pot Synthesis

The Cu-enriched Ir-Cu Nano-frames were synthesized by a one-pot synthesis strategy. [51]. In context to OER, they were found to be having more electro-catalytic activity. The main strategy behind Ir-Cu nanoframe synthesis was a galvanic replacement. $IrCl_3.3H_2O$, Cu $(acac)_2$ were dissolved in a solution of olylamine (surfactant, reductant) oleic acid (emulsifier), and octylamine (soft template reagent and solvent) under magnetic stirring. The resultant blue dark color solution was homogenous and transferred to Teflon lined stainless steel autoclave for 30 mins. The reaction conditions maintained were 170^0c and 24 hrs. Ir-Cu nanoparticles were synthesized. SEM, HRTEM, and HAADF-STEM analysis were used for the morphology assessment of prepared Ir-Cu nanoframes. XRD was used to determine the face-centered cubic (fcc) shape of bimetallic nanoframes. Elemental analysis was done by EDX. Lead sulfide nanoframes can be synthesized by the one-pot synthesis method. [52] Lead acetate trihydrate, oleic acid, and diphenyl ether were all mixed in a round bottom neck flask and degassed at 7^0c for 2 hours. During heating at 22^0c LiCl-DMF solution was added. TMA-DMF [thioacetamide dimethylformaldehyde] was then added to the mixture when the desired temperature was attained. When the solution became black immediately, it was an indication of PbS nanoframe formation as shown in (Figure 7)

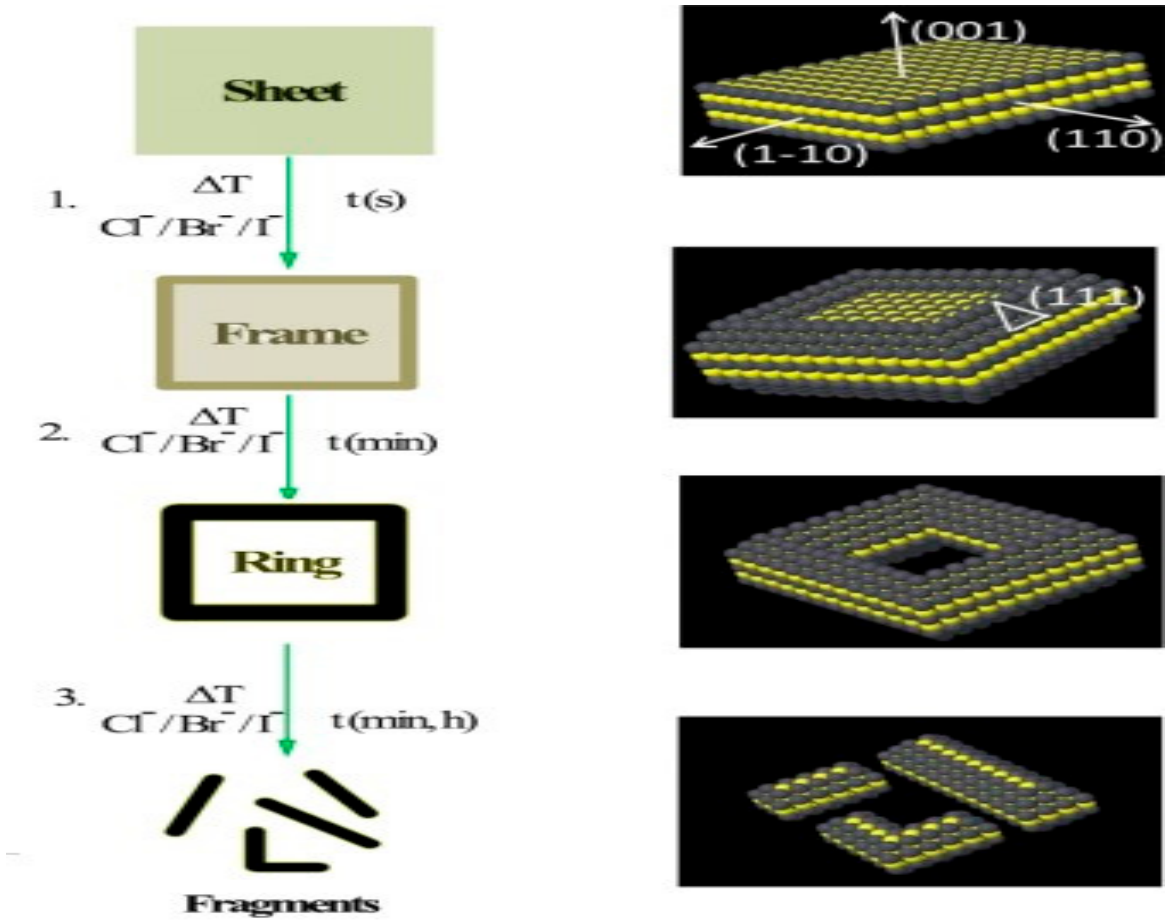

Figure 7. Crystallographic models of nanostructure designed by using lead (grey), Sulphur (yellow). (1) PbS nanosheet evolved into nanoframes (2) followed by nanoring formation (3) further decomposed into fragments prolonging the synthesis.

 doi:10.20944/preprints202401.2198.v1

Table 1. A summary showing different synthetic protocols that have been used to design different nanoframes.

Synthetic approach used	Metal	morphology	references
Nanocrystal face selected carving	Pt-Cu-Co	Rhombic dodecahedron	[30]
	Pt-Ni-Sn	Rhombic dodecahedron	[53]
	Au@Pd	cubical	[54]
Deposition of different metals on the template by preferentially edge-selection	Ru-Pd	Octahedron cuboctahedron	[55],
	Ir-Cu	Rhombic dodecahedron	[51]
	Ag-Au-Pt	cube	[56]
Hollow nanocrystal's dealloying	Ir-Cu-Au	Rhombic dodecahedron	[51]
	Pd-Au	Cube truncated octahedron	[57]
	Pt-Au	Cube truncated octahedron	[57]
Template-assisted arrangement of nanoscale building blocks	Au	Triangle, tripod	[58]
Directed deposition of nanoframe	Pt-Au@Au	Double-layered triangle, ring, hexagon	[48]
	Pt-Ni@MOF	Rhombic dodecahedron	[50]

2.6. Thermal Reductions

The 2D nanoframes of (Ni-Pt) were prepared by controlling temperature during the deposition of platinum on nickel hydroxide sheets [59]. Ni-Ir 2D nanoframes were synthesized in various steps including [60]. Firstly, the formation of nickel hydroxide nanosheets secondly, temperature-controlled treatments to synthesize nickel oxide nanosheets, thirdly, the deposition of Ir onto the previous nanosheets. Fourthly, thermal treatments (200/300^{0}c), lastly chemical leaching was done under certain conditions to finally form a Ni-Ir nanoframe as shown in (Figure 8)

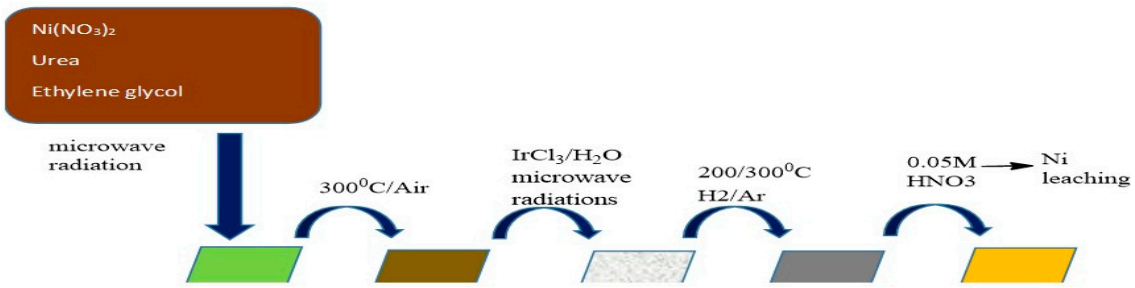

Figure 8. Schematic illustration of the experimental steps to synthesize 2D Ni-Ir nanoframes.

2.7. Oxidative Etching

It is one of the very important methods in the shape or stability control of nanomaterials with the help of an etchant. First of all Pd-Ru nanocrystals were formed by firstly preparing Pd seeds of 10nm followed by mixing of PVP, KBr, and Ru [III] precursor in triethylene glycol [TEG] and then heated to further initiate a reaction. TEM analysis has shown the monodispersity and octahedral shape of these nanocrystals as shown in (Figure 9A) [61].To determine the spatial distribution of both metals in Pd-Ru cuboctahedra EDX analysis was done (Figure 9C) It shows that within the core of the nanocrystal, Pd atoms were there. Whereas, at the corners and edges Ru atoms were distributed. When these nanoframes were subjected to oxidative etching in the presence of Br ions, it results in the etching of Pd as Ru is more resistant to oxidative etching. The ICP-MS analysis confirms that the

 doi:10.20944/preprints202401.2198.v1

weight percentage of Pd decreases from 69.1% in octahedral to 6.6% in nanoframe whereas Ru increases from 30.9% to 93.4%.

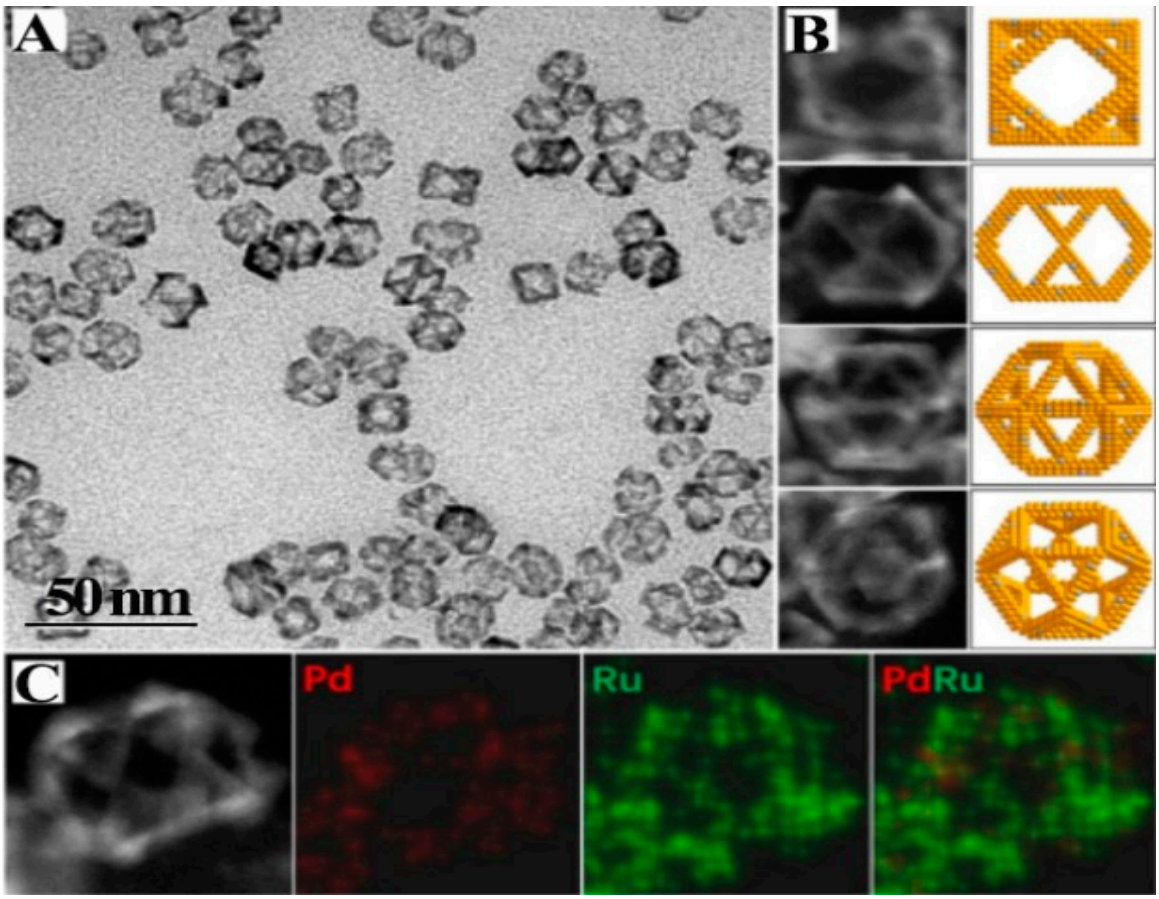

Figure 9. (A) TEM images of Ru cuboctahedral nanoframe (B) HAADF-STEM images viewed from different directions [100], [110], [211], [111] directions respectively (C) EDX mapping of individual nanoframes.

Other metal nanoframes can be synthesized like PtNi can be synthesized by the same method. [62] by this oxidative etching method. The metal precursor used was $H_2PtCl_6 \cdot 6H_2O$, Ni $(acac)_2$, and HAD(hexadecylamine) serve as reducing agents, surface ligands, and solvents. Initially, the platinum metal precursor was mixed with HDA at 20^0c. After that Ni precursor was added to a solution containing Pt seeds, heating the solution at 20^0C for 25 minutes PtNi nanoparticles of rhombic dodecahedral shape will be formed. EDS shows that on the corner and edges Pt was in more proportion while in bulk Ni was there. Using acetic acid as an etchant theses nanoparticles were converted into PtNi dodecahedral nanoframes (Figure 10) as confirmed by TEM analysis.

Figure 10. Schematic illustration for the synthesis of Pt-Ni dodecahedral nanoframe.

 doi:10.20944/preprints202401.2198.v1

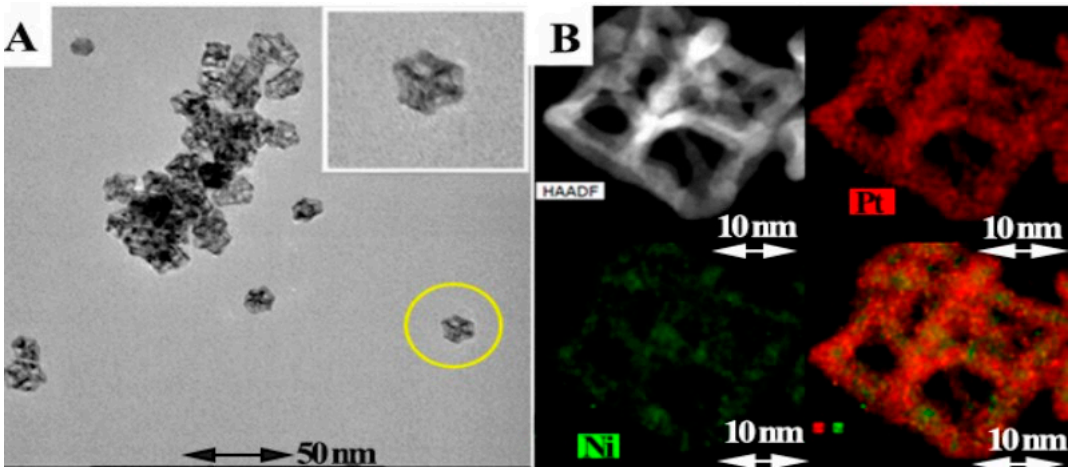

Figure 11. (A) TEM images of Pt-Ni dodecahedral nanoframe (B) HADF-STEM images and EDX mapping of Pt-Ni dodecahedral nanoframe.

2.8. Galvanic Replacement Reaction

Galvanic replacement occurs between two metals with different values of standard reduction potential. The one present in the metal template has low reduction potential hence it is oxidized while the one present in the solution has high reduction potential and hence it gets reduced and deposited on the template metal surface [53]. For example, Pt@Ru dodecahedral nanoframes can be synthesized by galvanic replacement reactions. What happen, initially Pt@Ni dodecahedral [precursor] was taken, and Ru was made to deposit on Pt edges by the replacement of Ni by the addition of $Rucl_3$, and the etching of Ni was done by using HCl as an etchant. Consequently, hollow Pt@Ru dodecahedra will be formed as shown in (Figure 12) [63]. TEM and SEM images are shown in (Figure 13).

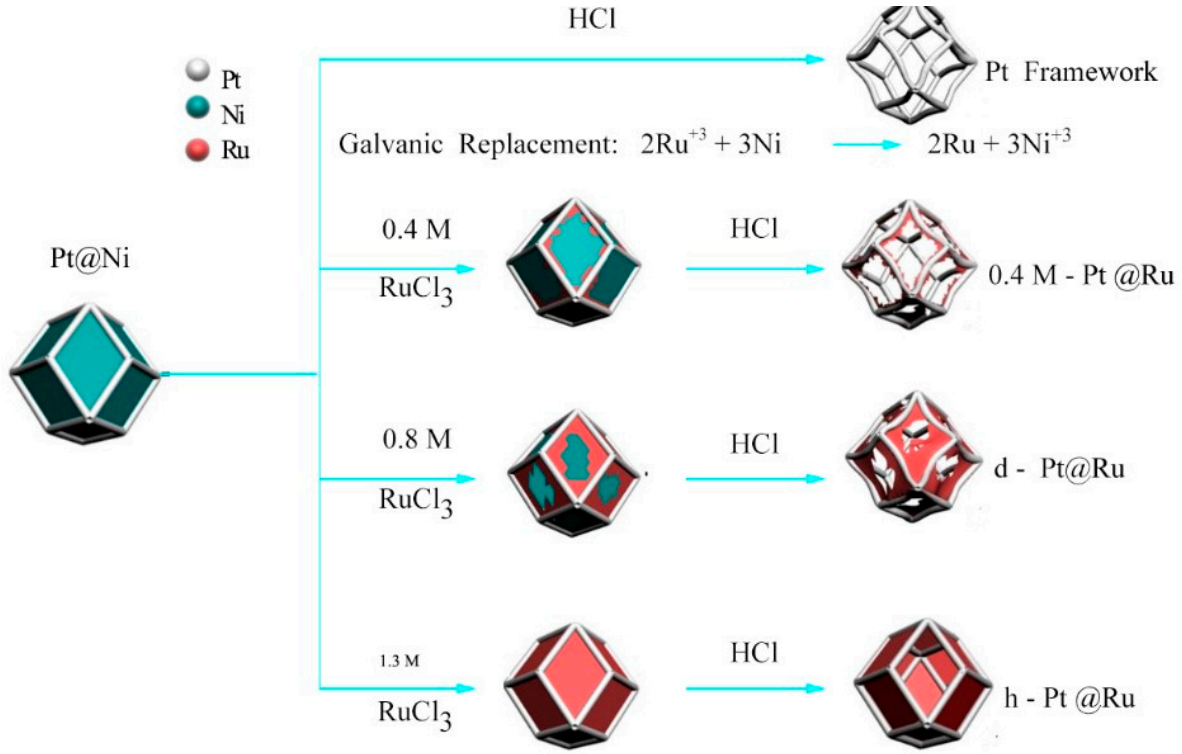

Figure 12. Scheme of the synthetic routes for tunable hollow Pt@Ru nanoframe.

 doi:10.20944/preprints202401.2198.v1

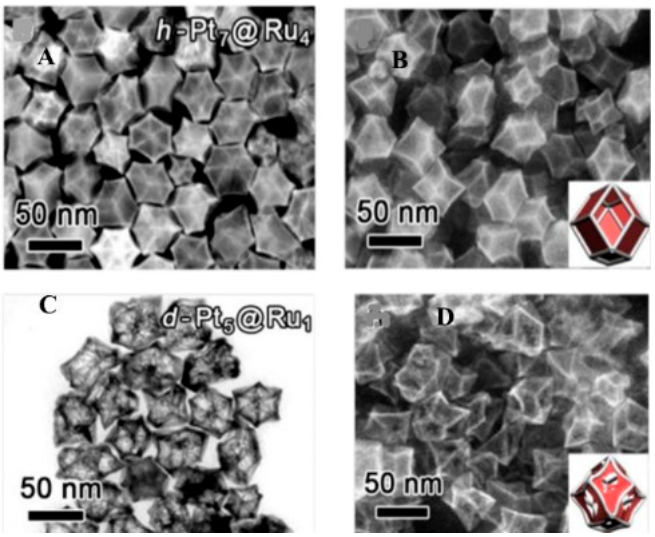

Figure 13. (A, B) TEM dark field image and SEM image of h-Pt@Ru (C.D) TEM bright field image and SEM image of d@Ru. Insets are corresponding structure models.

2.9. Kirkendall Effect

It is a technique mediated by vacancies in which the flow of faster diffusing species is stabilized by the antagonistic flow of vacancies [64]. This method is not usually used to synthesize metal alloy nanoframes. However, the synthesis of nanoframes reported in the literature by this method includes Cu_3Pt NFs and some trimetallic nano boxes like Pd-Au-Ag nano box [65]. Successive Galvanic Replacement and Kirkendall effect can be done to design complex hollow nanostructures ie Pd-Au-Ag hollow nano box. In this context, two stages are required (Figure 14) In the I stage, a metal precursor with high reduction potential (Pd) is needed to create cavities in metal nanoparticle (Ag). CTAB was used as controlling agent. In stage II the already designed hollow structure was used as a support for 2nd carving by using gold as metal precursors to create further strained cavities. Now Ascorbic acid was used as a controlling agent.

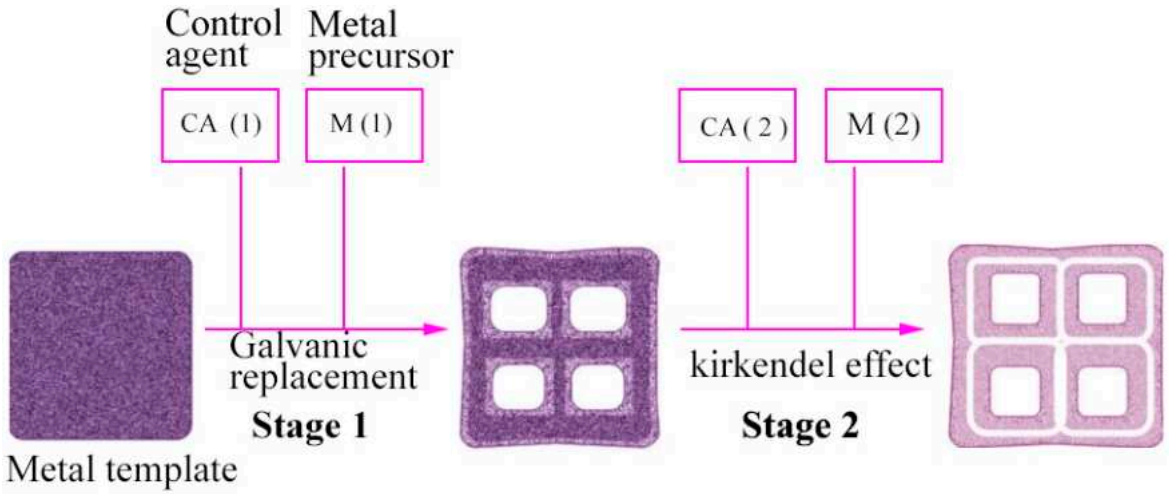

Figure 14. Synthetic protocol to complex polymetallic hollow nanomaterials by galvanic replacement followed by Kirkendall effect.

2.10. Photocatalytic Template Synthesis

3D Pt nanocages have been successfully prepared by photocatalytic template synthetic protocol (Figure 15). First of all platinum nanobranches were deposited on titanium oxide NPs in the presence

 doi:10.20944/preprints202401.2198.v1

of UV radiation (UV-340A) for almost one and a half hours and non-stop magnetic stirring. When templates were removed, platinum nanocages [NCs] were acquired. These NCs were found to have good electrocatalytic stabilities in the case of methanol oxidation reaction explored by chronoamperometric analysis [66]. TEM images at different growth stages are shown in (Figure 16)

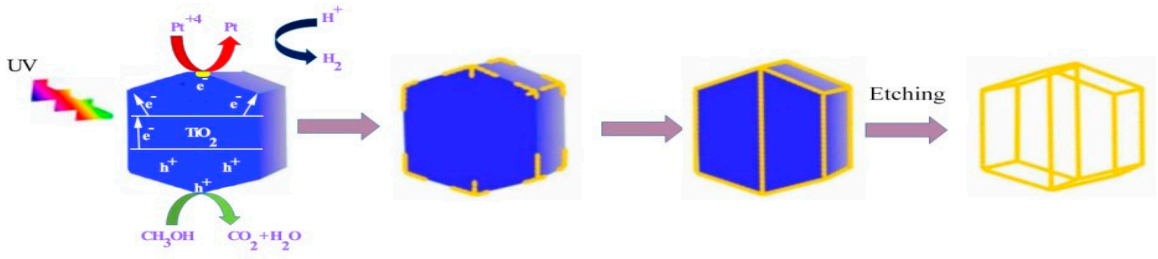

Figure 15. Schematic representation of pt nanocubes by photocatalytic template synthesis.

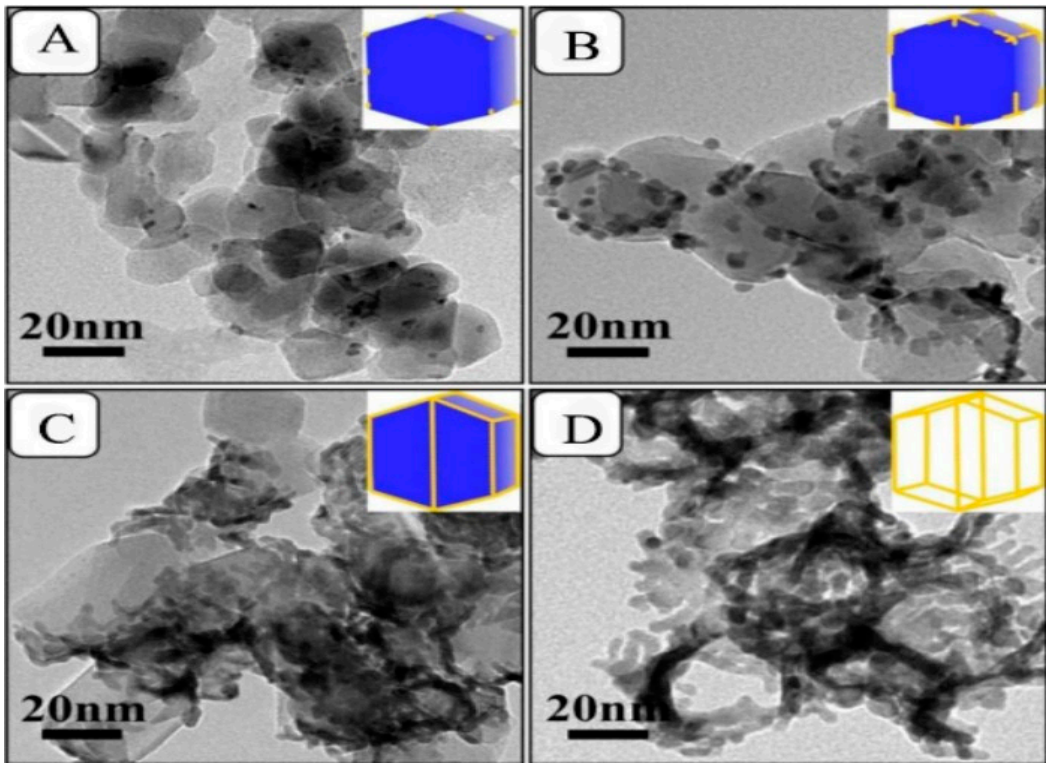

Figure 16. TEM images of Pt-200 samples assembled at a different times of growth stages (A) 30 mins (B) 60 mins (C) 90 mins (D) Pt nanocage.

2.11. Self-Assembly of Nanoparticles

MD simulations were used to explain this synthetic protocol in which first of all, nanoparticles acting as building blocks were annealed at high temperature, and the metal nanostructures obtained at the end were cooled at 10K. Silver-gold nanoframes were synthesized by the self-gathering of almost 12 similar 5083-atom of Ag-Au NPs. At 1000K, an annealing MD simulation was performed. At 50ps, just gathering of NPs took place into triangular Ag-Au nanoframe, and finally at 100ps triangular nanoframe was formed and by the same method, hexagonal gold NFs (Figure 17) and cubic Fe NFs were also synthesized. [22]

 doi:10.20944/preprints202401.2198.v1

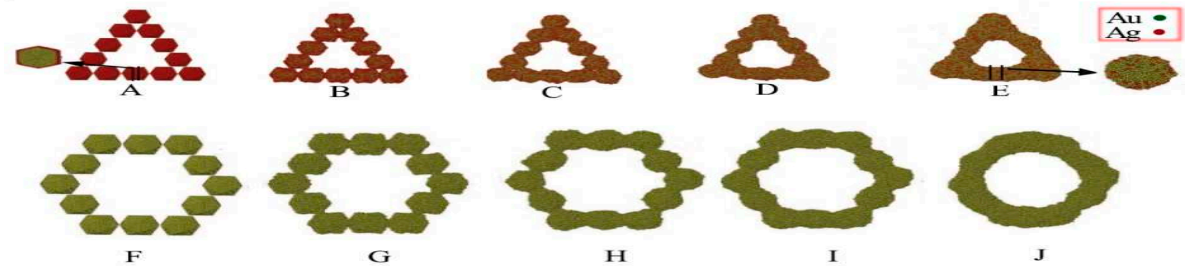

Figure 17. Evolution models of triangular Ag/Au nanoframe (A-E) and hexagonal Au nanoframe (F-J).

2.12. Solvo-Thermal Synthesis

It is a technique in which the precursor material is mixed in a proper solvent and then heating it at a temperature greater than its boiling point after sealing it in an autoclave. Synthesis of ptCu dodecahedral NFs has been reported by this method. The solution containing CTAC (cetyltrimethyl ammonium chloride), olylamine, $CuCl_2$, and allantoin was first stirred and then ultrasonicated for 40 mins followed by transference of mixture to autoclave at 180^0C for 10 h and allowed it to cool down naturally. [67] Afterward, centrifugation, washing, and drying at 60^0C were done. A schematic illustration for dPtCu nanoframes is shown in (Figure 18).TEM images are shown in (Figure 19)

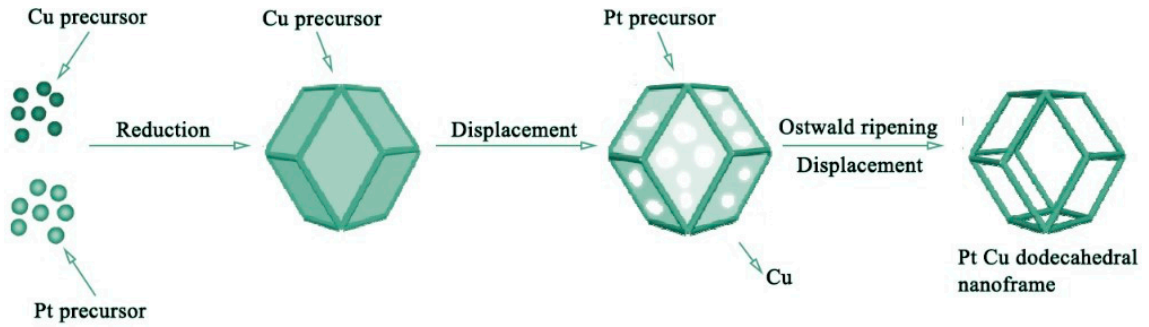

Figure 18. Mechanism of dPtCu nanoframe formation.

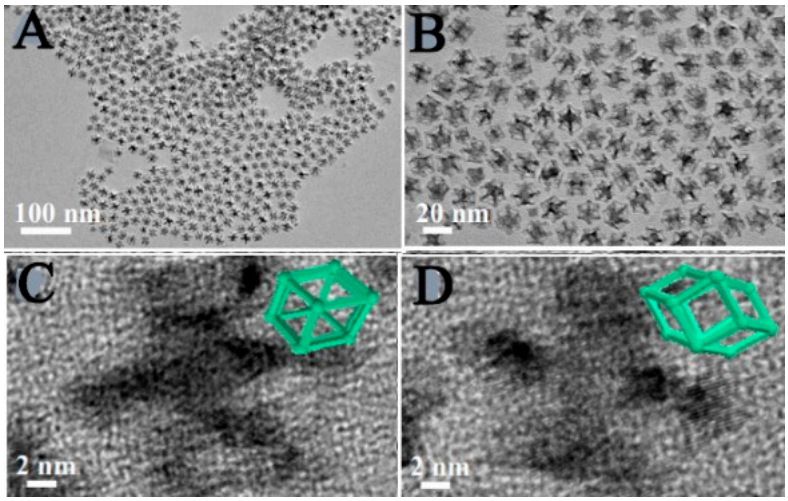

Figure 19. (A) Low (B) medium (C,D) high resolution TEM images of dPtCu nanoframes.

Rhombic dodecahedral ptCu NFs synthesis has also been reported by this method by using CTAC, OAm, and L-proline [68]. PtCu octopod nanoframe architectures OFAs (Octopod nanoframe architectures)were also synthesized by this method [69]

 doi:10.20944/preprints202401.2198.v1

3. Different Metal Nano-Frames

3.1. Metal Nanoframe

A novel structure containing Au films deposited by Ag nanoframes was checked for the SER effect [70]. It was reported that intense SERS signals were shown by Ag nanoframes Au film sample whereas no such response was observed for Au film without Ag nanoframes. This substrate was found to be a suitable material for the identification of material in the biological domain.

3.2. Alloy Metal Nanoframe

For electro-oxidation catalytic performance pt-Cu, nanoframes were investigated in two different morphologies named ($PtCu_2$ CONFs) and (PtCu UONFs) abbreviated as $PtCu_2$ concaved octopod nanoframes and $PtCu_2$ ultrathin octopod nanoframes respectively [29]. The ECSA CONFs, UONFs, pt/C, and pt black were found to be 44.5 m2 /g, 52.1 m2 /g, 46.1 m2 /g, and 41.4 m2 /g respectively. Due to its small size and greater access into the inner area of nanoframes, PtCu UONFs exhibited superb electrochemical performance comparatively. ptNi dodecahedral nanoframes have been prepared by oxidative etching method from already design precursors like ptNi rhombic dodecahedron nanoparticles. The specific activity of these nanoframes for ORR was found to be 1.9 $mAcm^{-2}$ which was greater than the commercially available Pt/C specific activity i-e 0.19 A·mg-1. [62] Ni-Pt nanoframes (2D) were also synthesized from Pt containing $Ni(OH)_2$ nanosheets. The ORR-specific activity for these nanoframes was found to be (5.8 mA $cmPt^{-2}$) much greater than the Pt/C catalyst [71] icosahedral pdRu nanoframes [72]. Ru octahedral nanoframes were prepared from the octahedral structure of the Pd-Ru core frame by preferential etching of Pd cores. As compared to Ru nanowires, their fcc nanoframes morphology was found to be most suitable for the degradation of p-nitrophenol. [73]. Another category of nanoframes includes porous metal oxide nanoframes like manganese tin oxide nanoframes. They were analyzed to enhance Li-ion storage abilities. Their initial capacity was found to be 1620.6 mA h g^{-1} at 0.05 A g^{-1} and their durability was so high that they were capable to transport a capacity of 547.3 mA h g^{-1} at 2 A g^{-1} despite one thousand cycles [74]. Some yolk-shell nanoframes like $Ag@mSiO_2$ with Ag NPs as yolk and glucose oxidase conjugated mesoporous silica as shell, have been prepared to investigate for cancer treatment. The experimental results showed that the glucose oxidase was found to be the basics of nanocarriers which were mainly responsible to trigger the entire approach. These NFs had given the marvelous result for cancer-killing effect and efficient cellular-uptake ability. [75]

3.3. Doped Metal Nanoframes

Copper nanoframes were found to be having a much better performance for ORR. It was reported that the half-wave potential for Cu ISs/NC-1000 (copper isolated sites anchored on nitrogen-doped carbon material) was 0.92 V which was much more efficient as compared to commercially available Pt/C. [76]

4. Applications

4.1. Electro Catalytic Performance

4.1.1. MOR

The nanoframes named as d-Pt@Ru and h-Pt@Ru are analyzed for their efficient electrocatalytic activity for methanol oxidation. [63] For this purpose, these hollow nanoframes are carried on (MWCNTs) with their 20wt% loading. Their activity for methanol oxidation was checked for different Pt-Ru nano-samples by using H_2SO_4 and CH_3OH. Their catalytic efficiency was detected initially by ECSA (electrochemical surface area) which in turn was estimated from the hydrogen-desorption region of CV curves (Figure 20A). Among all the samples analyzed, the highest mass activity was possessed by d-Pt@Ru dodecahedra i-e 0.80A $mgpt^{-1}$ and specific activity was found to be 1.61mA

 doi:10.20944/preprints202401.2198.v1

cmpt^{-2}. (Figure 20B) In comparison to commercial Pt/C, d-Pt@Ru dodecahedra were found to be 5.25 and 7.78 times more efficient in mass activity and specific activity. The d-Pt@Ru and h-Pt@Ru were also tested for their anti-poisoning ability which ensures their enhanced electro catalytic ability. In addition to this material, the CV curves of PtCuRh RDND(ptCuRh-rhombohedral dodecahedron nanoframe with nanodentrites), PtCuRh RDN(rhombic dodecahedron nanoframe) PtCu NC and commercial Pt/C catalysts were analyzed and the peak current density was found to be 56.9 mA cm^{-2}, 56.0 mA cm^{-2}, 32.3 mA cm^{-2}, 25.76 mA cm^{-2} respectively. To find the durability of this material, a durability test was performed. For Pt/C and PtCu NC it was reduced up to 44% and 49% and PtCuRh RDND, PtCuRh RDN were able to maintain 73.2% and 60.6% of their original activity [77]

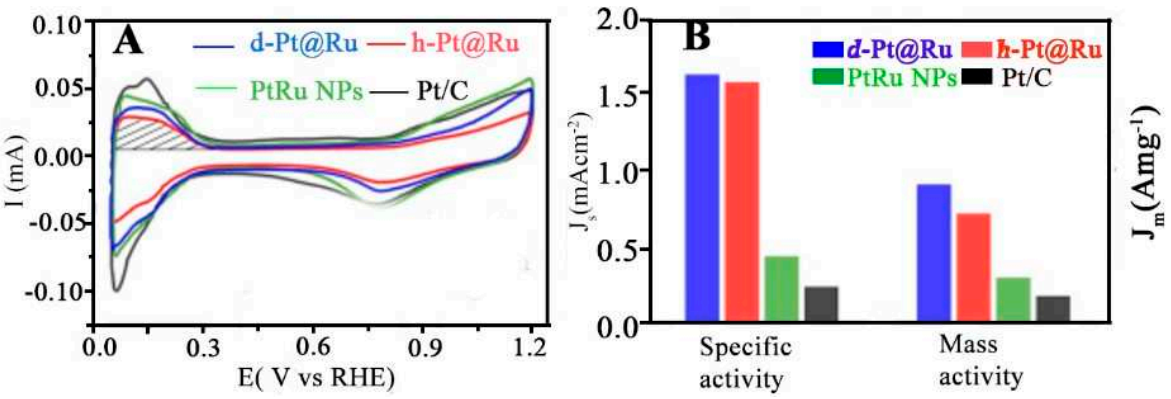

Figure 20. (A) CV curves of four different catalysts in 0.5M H2SO4 (B) Comparison of specific activity and mass activity at 0.8 V, V vs RHE.

4.1.2. EOR

For EOR, CV plots for PtCuRh RDND, PtCuRh RDN, PtCu NC, and Pt/C are compared (Figure 21A). It was estimated that PtCuRh RDND exhibited a maximum current density of 29.9 mA cm^{-2} and which is 2.3 times higher than commercial Pt/C catalysts. As far as mass activity is concerned it was calculated as (0.98 A mgPt $^{-1}$) for the former as compared to (0.48 A mgPt $^{-1}$) for the later [77]. There was found a 44% and 49% decrease in the mass activity of Pt/C and PtCuNc as compared to PtCuRh RDND, PtCuRh RDN which were quite durable to maintain their mass activity up to 73.2% and 60.6% of the original value even after 1000 cycles of stability test. (Figure 21B)

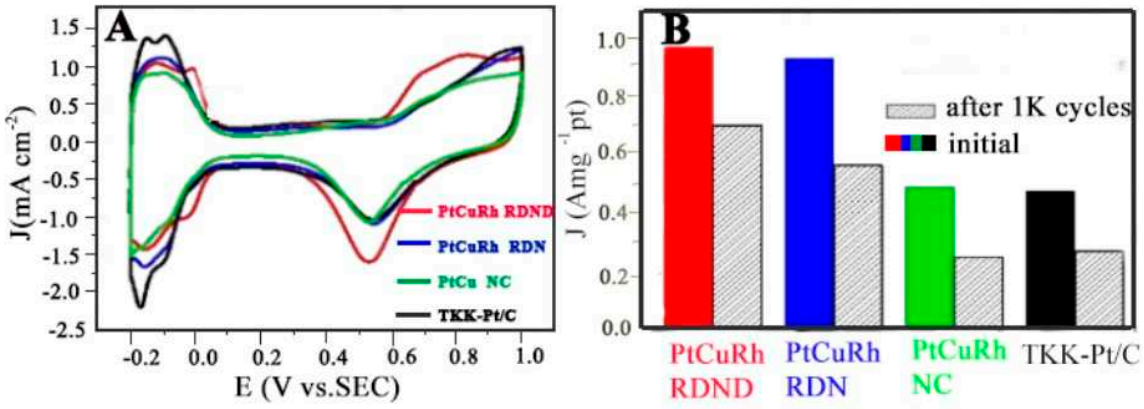

Figure 21. (A) CV curves obtained for e PtCuRh RDND, PtCuRh RDN, PtCu NC and Pt/C in 0.5M H_2SO_4 aqueous (B) Histograms of mass activity after 1000 cycles stability test.

 doi:10.20944/preprints202401.2198.v1

4.1.3. ORR

The ORR activity of $Ni(OH)_2$@Pt was detected by using RDE (rotating disc electrode). In the NiPt-200 and NiPt-300 nanoframes, [71] the half-wave potential was found to be 70mv more positive than Pt/C. Their CV plots are shown in (Figure 22A). The specific activity was found to be 3.2 ± 0.6 and 5.8 ± 2.4 mA $cmPt^{-2}$ respectively which shows that NiPt-300 nanoframe was found to be 10.2 times more efficient than Pt/C (0.57 ± 0.03 mA $cmPt^{-2}$) in terms of a specific activity (Figure 20B). The increased specific activity of NiPt-300 as compared to NiPt-200 might be due to many factors like the complete transformation of $Ni(OH)_2$ that took place in its structure, and the presence of micropores. The decreased mass activity of NiPt-300 and NiPt-200 nanoframe in comparison to Pt/C is just because of less ECSA of Pt with NiPt nanoframes.

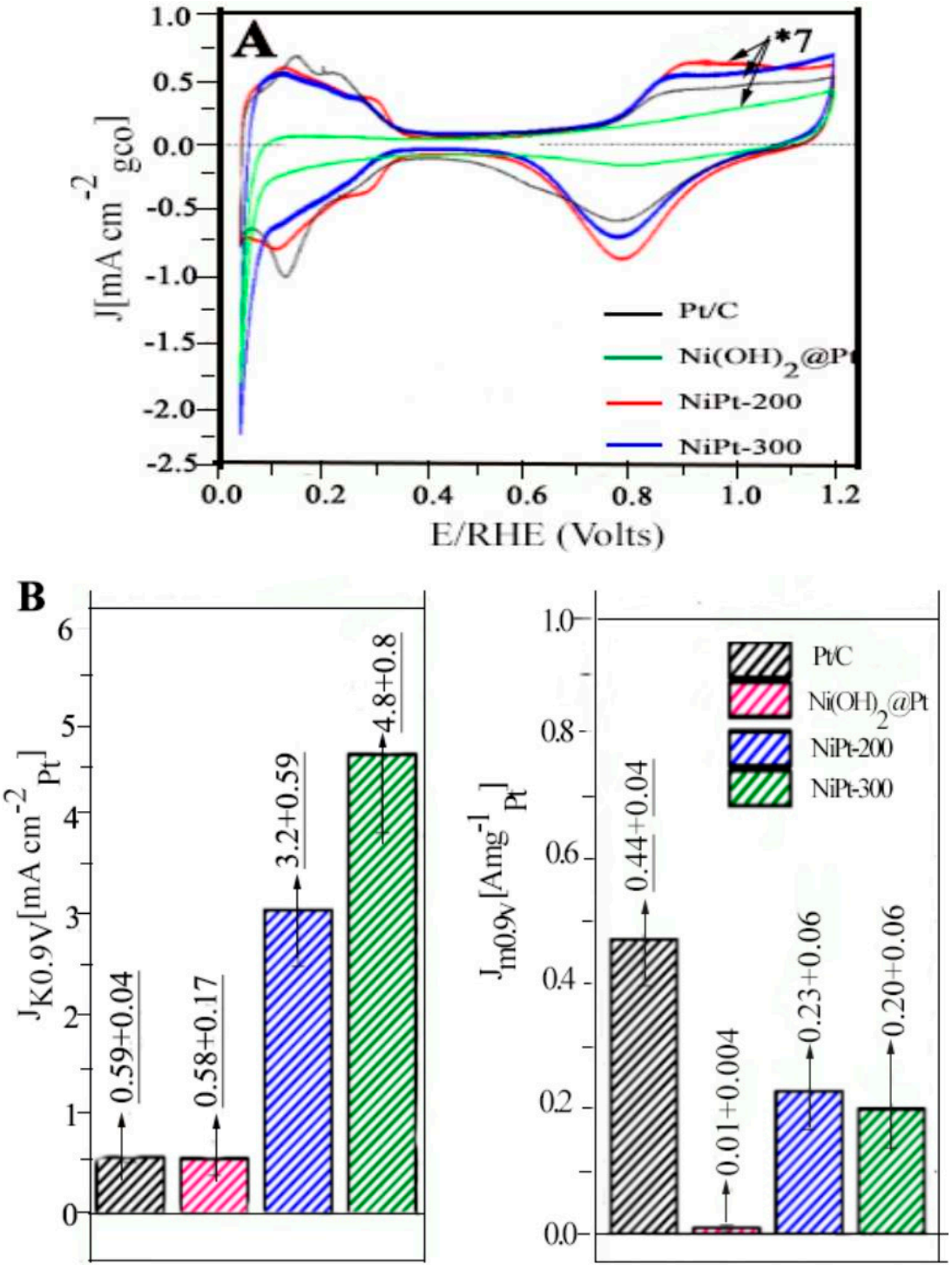

 doi:10.20944/preprints202401.2198.v1

Figure 22. (A) CV,The current for unsupported NiPt-200 and NiPt-300 2D nanoframes, Ni(OH)2@Pt is multiplied with factor 7 to facilitate the comparison with state-of-the-art catalyst i-e Pt/C (B) comparison of specific activity NiPt-200 and NiPt-300 2D nanoframes, Ni(OH)2@Pt, and commercial Pt/C (left) mass activity (right).

4.1.4. HER

Different metal nanoframes like PtCu DNFs (dodecahedral nanoframes) have been investigated for enhanced HER. To analyze their electrocatalytic performance CV graphs of different samples like PtCu DNFs, PtCu NPHs, Pt/C, and Pt black catalysts were studied (Figure 23A) [67]. The onset potential determined through the Tafel slope shows that it is more positive (0mV) for PtCu DNFs as compared to -20mV, -21mV, -36mV of Pt/C, PtCu NPHs, and Pt black respectively which is a clear manifestation of increased HER performance of the earlier (Figure 23B). The over potential value for all the above-mentioned different catalyst structures was found to be 27 mV, 37 mV, 66mV, and 78 mV, depicting very efficient electron transfer at dodecahedral nanoframe structure.

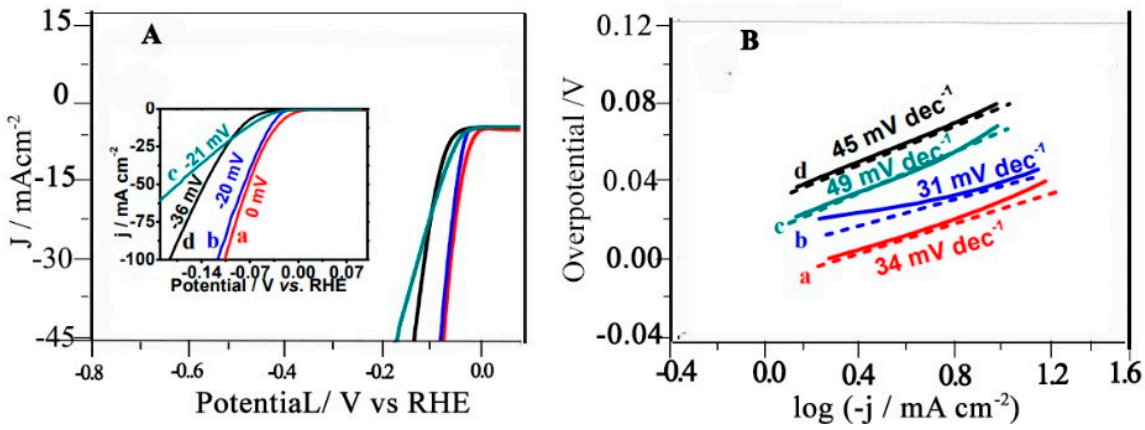

Figure 23. Comparison of electrochemical properties f PtCu DNFs (curve a), Pt/C (curve b), PtCu NPHs (curve c) and Pt black (curve d), 0.5 M H_2SO_4,Scan rate 5mVS^{-1} (A) HER polarization curves (B) Tafel plot.

4.1.5. Formic Acid Oxidation Reaction (FAOR)

Palladium nanoframes were found to be an efficient catalyst for formic acid oxidation. Formic acid can be used as fuel in fuel cell technology. CV graphs of two catalysts were analyzed for electro-oxidation of formic acid, and Pd NFs were showing 7.5 times more activity in comparison to Pd octahedral catalyst (Figure 24A) [40]. As far as electrochemical durability after 1000 cycles were checked, it was found to be 6.5 times higher for Pd nanoframe as compared to Pd octahedral.(Figure 24B)

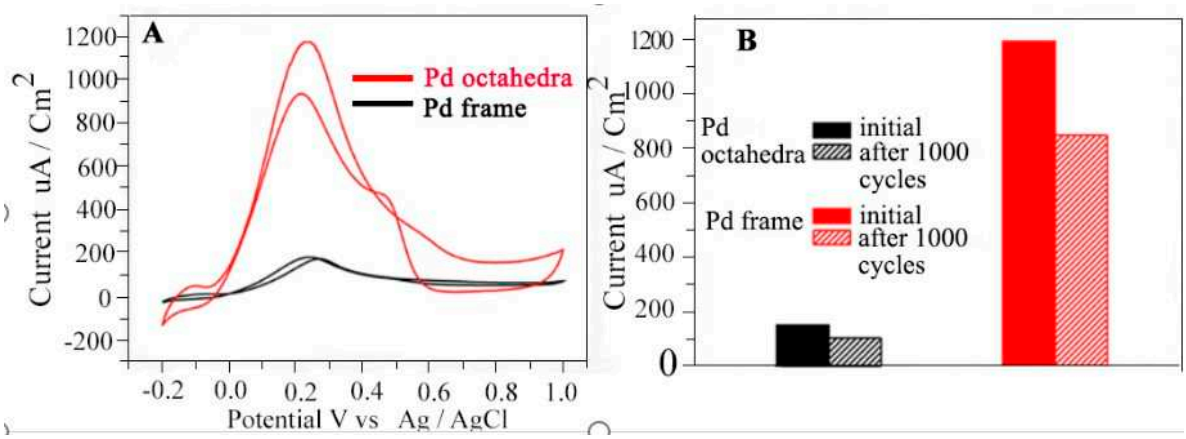

 doi:10.20944/preprints202401.2198.v1

Figure 24. (A) CV curves of Pd nanoframe and Pd octahedra normalized against ECSA (B) Electrochemical durability test after 1000 cycles.

4.1.6. Overall Water Splitting

CoP nanoframes were found to possess the best catalytic activities for HER, and OER [78]. Besides this, they were also having both water reduction and oxidation properties or in short water splitting ability. [78] The LSV curves for CoP NFs and CoP NCs showed that cell voltages of 1.65 and 1.75 V were required to acquire a current density of 10mAcm^{-2} for water splitting (Figure 25A). As far as durability is concerned the water splitting ability remained constant even after 30h. (Figure 25B). Transition metal phosphide (TMP) 3D nanoframes were found to best material for overall water splitting [79] another metal nanoframe (Ni, C0)$_2$PNF was used as both anodic and cathodic material for overall efficient water splitting [80]

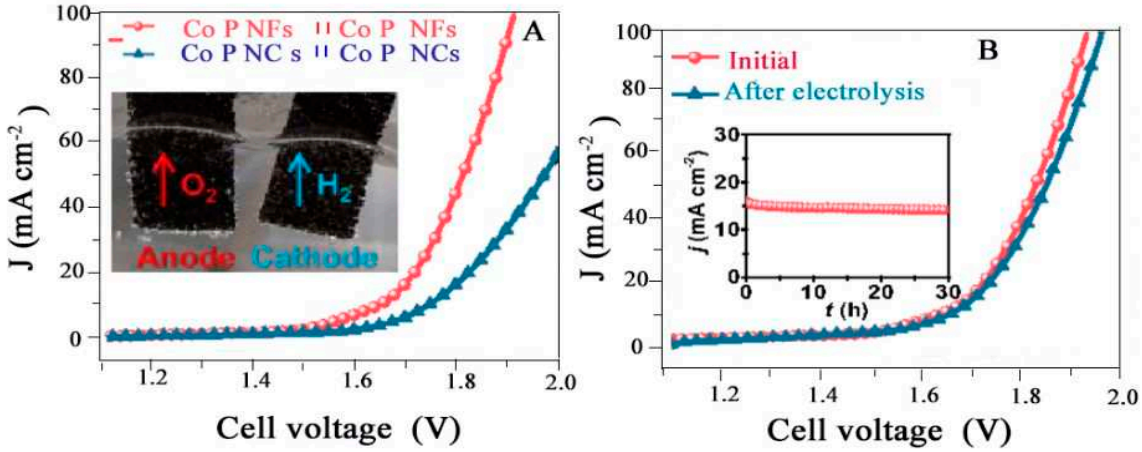

Figure 25. LSV curve of CoP NFs|| CoP NFs and CoP NCs||CoP NCs (A) in 1 M KOH without iR compensation in two electrode configuration (B) before and after electrolysis in 1M KOH.

4.1.7. GOR

PtCu HCNFs were declared as the best catalyst for GOR: [81] as compared to other catalysts observed under the same conditions. It was demonstrated that there happened a diffusion-controlled process on the surface of the catalyst for GOR. The slope value of CV plots for Pt-HCNFs (Pt Cu alloyed hollow cubic nanoframes), Pt-NCs (Pt nanocubes), and Pt/C was calculated as 12.8,6.2,2, and 2.6 respectively. The ECSA of PtCu-HCNFs, Pt black, PtCu NPs was calculated as 23.4 m ^{2} g $^{-1}$ Pt, 12.04 m ^{2} g $^{-1}$ Pt, and 15 m ^{2} g $^{-1}$ Pt respectively (Figure 26A). Moreover, the ORR polarization curve depicts enhanced stability and activity towards ORR (Figure 26B) the PtCu-HCNFs were considered to possess enhanced electrochemical performance towards GOR [82].

Preprints.org (www.preprints.org) | NOT PEER-REVIEWED | Posted: 31 January 2024 doi:10.20944/preprints202401.2198.v1

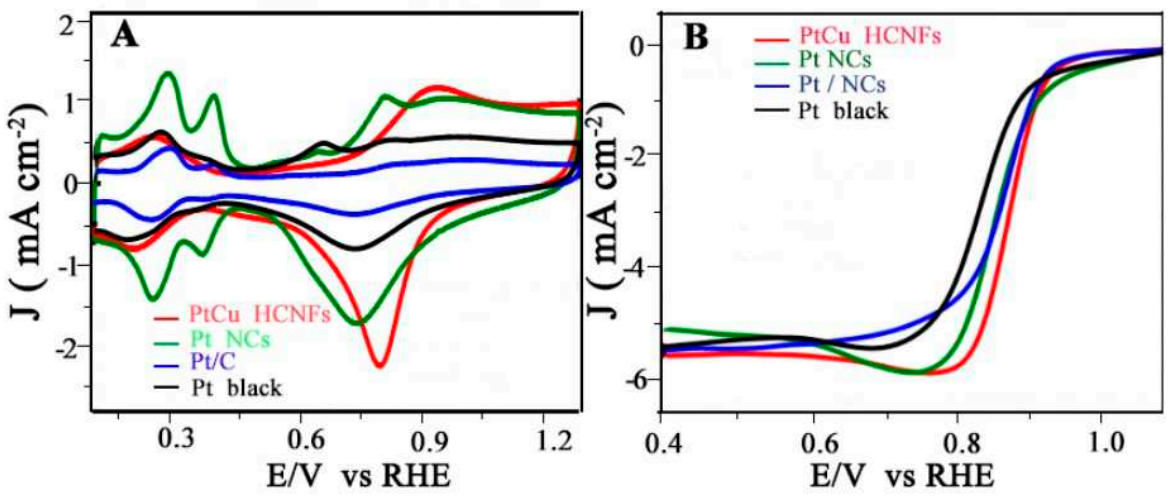

Figure 26. Electrochemical properties of_PtCu HCNFs, Pt NCs, Pt/C, and Pt black catalysts in 0.5 M KOH at 50 mV s^{-1}.(A) CV plots (B)ORR polarization curves.

4.2. Biomedical Applications

4.2.1. Healing of Liver Injury

Gold nanoframes have been analyzed for in-vivo biomedical applications due to their increased physiological stability and efficient biocompatibility [83]. C57BL/6 female mice were used as a model to evaluate liver injury by intravenous injection of different nanostructures like GNSs (gold nanoshells) and GNFs (gold nanoframes). The portion of the liver treated with GNSs showed the existence of inflammation over there. The causative agent responsible for this inflammatory response was oxidative stress due to the enhanced assembling of GNSs which in turn increases ROS production. As opposed, the same concentration of GNFs did not cause any unusual biological changes at the portion of the liver where they were inducted. In addition to the liver, the experiment was also performed on the spleen, kidney, and lungs by doing 24-h post-injection of GNFs and no unusual changes were observed. In comparison to GNSS, GNFs not only have excellent physiological stability but also efficient stability. (Figure 27) Hence GNFs can be suggested as the best material in the future for in-vivo utilizations like cancer detection etc.

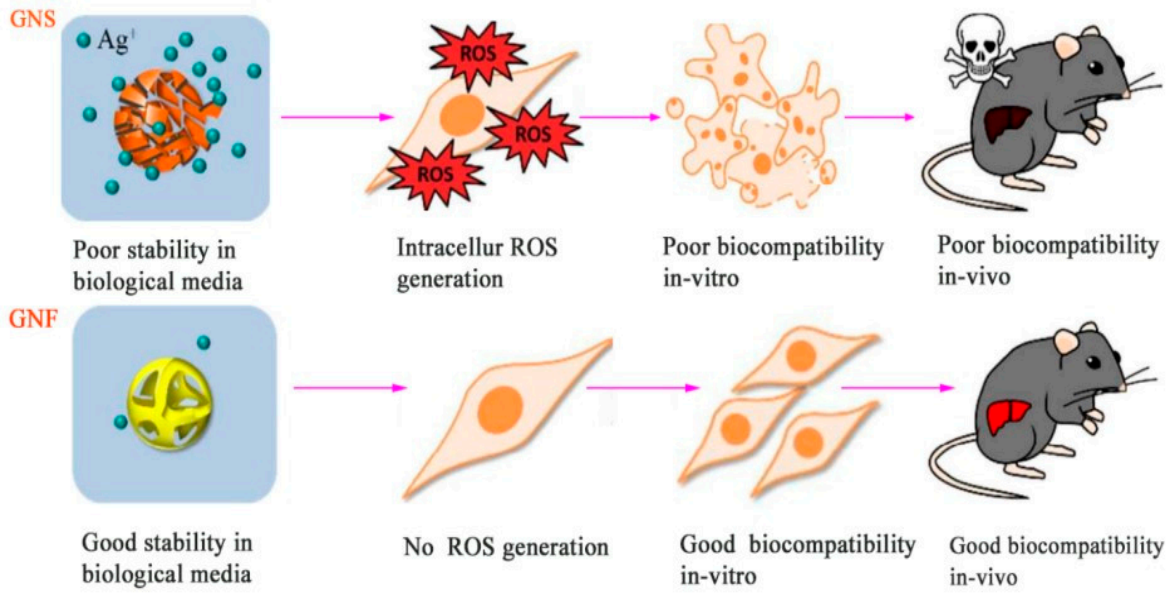

 doi:10.20944/preprints202401.2198.v1

Figure 27. Schematic illustration to compare physiological stability and biocompatibility of GNs and GNFs.

4.2.2. Detection of Tumor Cells

To achieve excellent sensitivity and detection of cancerous cells, there is a need to further amplify the detection signals. For this purpose detection signals were converted into temperature and pressure signals by using novel (NIR-II) responsive Au-NFs [84]. NIR absorption spectra of different Au-NFs system is shown in (Figure 28A). The production of CO_2 and NH_3 and O_2 as a result of the disintegration of H_2O_2 and photo thermal conversion of NH_4HCO_3 enhances pressure signals and its peroxidase activity to TMB (3,3 5,5 tetremethylμ benzidine) to TMB oxide (oxTMB) further improves its photo thermal response. The pressure and temperature signals were found to be linearly correlated with Au-NFs concentration. The system containing Au NF,TMB, H_2O_2 has shown improved signals with temperature changes (Figure 28B).To investigate clinical applications Hela cells were introduced into human serum and blood samples, Au-Nfs were found to have good biocompatibility as the hemolysis rate calculated was only 5%. The LOD determined for both temperature and pressure signals through this nanoframe was found to be very low than the other methods already reported i-e electrochemistry [85,86] mass spectrometry [87,88], optics [89].Au@Au–Ag DCFs (Au@Au–Ag dot in cubic nanoframes) have also been reported for asymptomatic SERS and photoacoustic detection of tumors with a detection depth of up to 4mm. [90]. The SERS images become brighter with increasing Au@Au–Ag DCFs concentration (Figure 29A1) Moreover SERS intensity increases with its increased concentration (Figure 29A2).it was analyzed that SERS images become darker with increasing depth and SERS intensity was found to be decreased with increasing depth(tissue mimicking thickness) of detection (Figure 29B1,2).

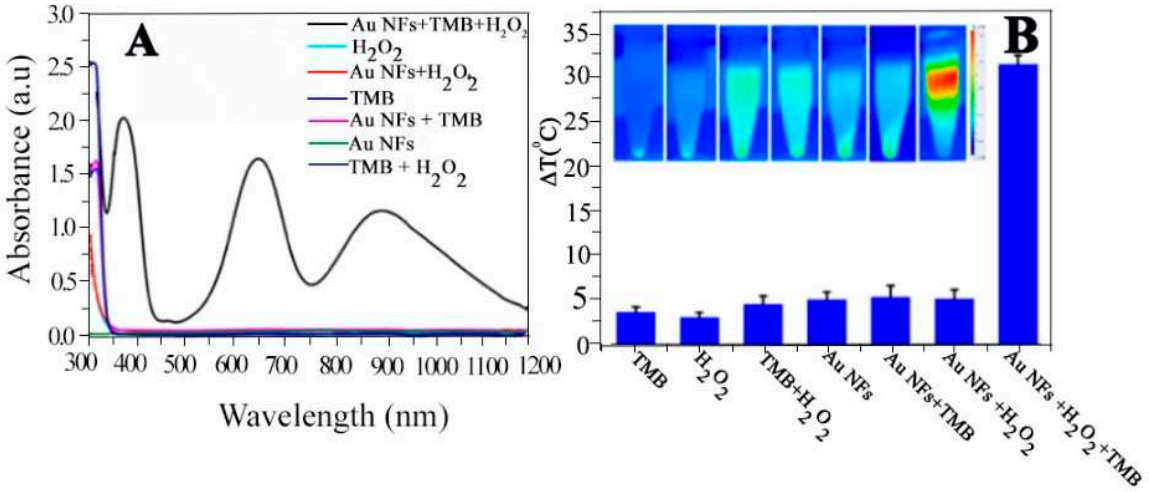

Figure 28. (A) UV-Visible NIR absorption spectra of Au NF-mediated TMB-H2O2 system (B) Temperature changes of different Au NF-mediated TMB-H_2O_2 system.

 doi:10.20944/preprints202401.2198.v1

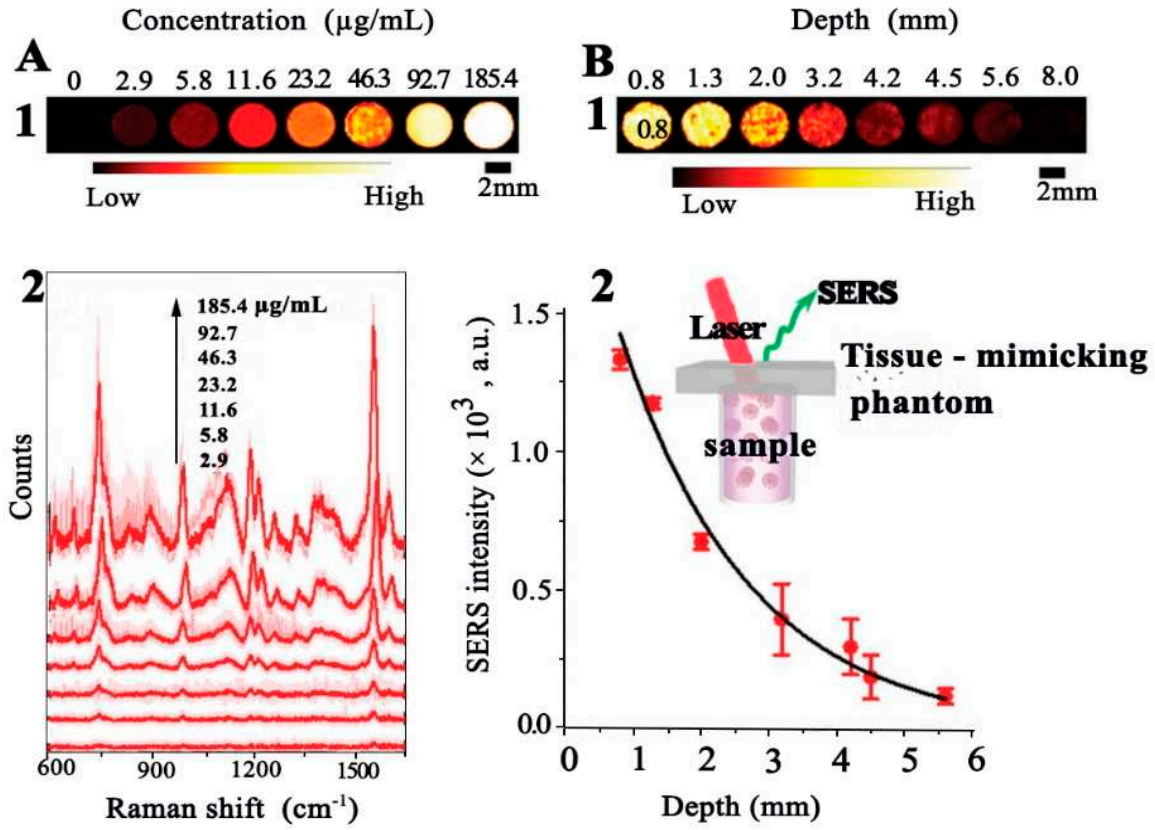

Figure 29. (A) 1-SERS images Au@Au–Ag DCFs at different penetration depths, 2- SERS spectra of agarose phantom containing different concentrations of f Au@Au–Ag DCFs (B) 1- NIR-II SERS images of the agarose phantoms containing 185.4 μg mL−1 Au@Au–Ag DCFs at different penetration depths 2- the decay of the average NIR-II SERS intensity over the increasing penetration depth under 1064 nm laser (laser power: 13.1 mW; integration time: 5 s.

4.2.3. Synergistic Photo Thermal and Chemo Dynamic Therapy

Concave octahedral PtCu nanoframes were loaded with vitamin C to form CoPtCU-nfs@VC as an anti-tumor Nano agent. They were also modified with tumor-targeting folic acid CoPtCU-nfs@VC@FA [91]which can easily deliver VC to cancerous cell targets. These NFs were related to the generation of OH radical and H_2O_2 production which cause serious toxicity and damage to tumor cells. Its PC (photo thermal conversion) efficiency was found to be 68.4% with the only heat loss of 2% after performing 6 thermogenesis cycles. NIR laser irradiation at 880 nm showed quick release of model drugs (methylene blue and hydrophobic rhodamine) as compared to when no laser radiations were used. These NFs in combination with NIR showed better tumor volume reduction (Figure 30A) and survival rate of mice in comparison to other samples or combinations are shown in (Figure 30B)

 doi:10.20944/preprints202401.2198.v1

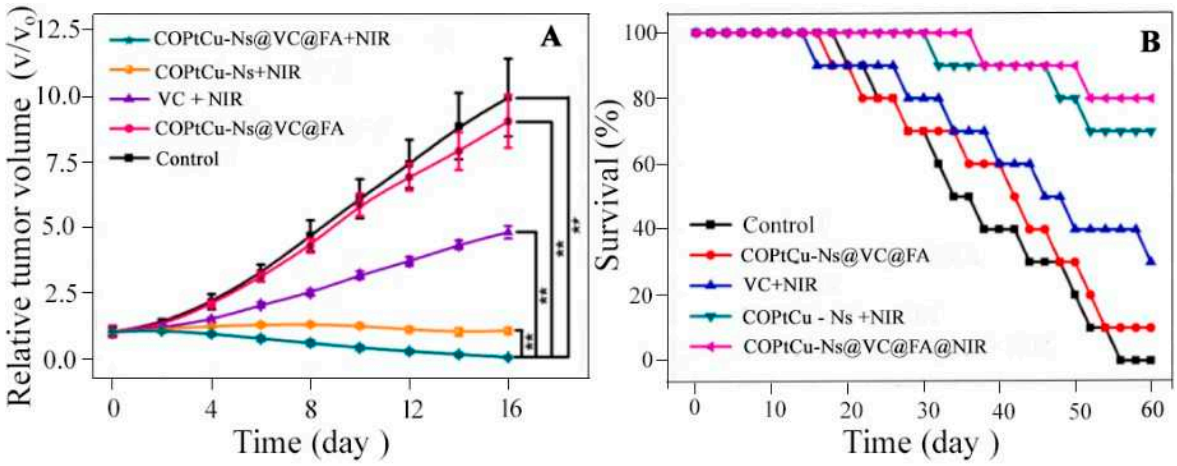

Figure 30. in vivo anti-tumor experiments (A) Relative tumor volume for various therapeutic treatments within 16 days (B) Survival rate of mice in various groups during 60 days period.

4.3. Theranostic Application

The combined strategy of therapeutic and diagnostic capabilities comes under the umbrella of theranostic applications. [92]. The combination of the experimental and theoretical analysis showed that on the surface of Au NFs and throughout their interior structure, intense plasmonic surface field effects occur in comparison to other solid nanostructures [93]. Due to the distinctive framework of NFs, their LSPR can be modulated to NIR from the visible region by changing the dimensions of NFs during synthesis, and this property makes them a promising candidate for in-vivo applications. In addition to that, they have appreciable sensitivity factors and hence they serve as the best material for Nano sensors in NIR. Optical response of nanoframes were investigated as a function of aspect ratio(R) and length (L). It is estimated that nanoframes with better absorbance in NIR are best for Theranostic applications. When L value increases, LSPR absorption also increases from 690 to 1060nm. (Figure 32A) As the R value increases, LSPR peak wavelength also increases from 600nm to 1090nm as R=L/W, L is kept constant (Figure 32B)

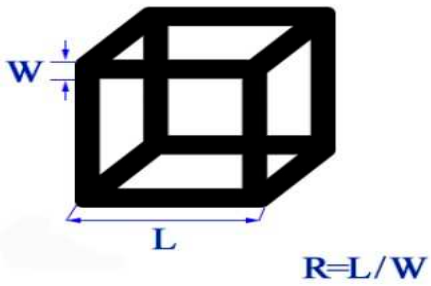

Figure 31. Nanoframe with different dimensions (L) edge length (W) Edge thickness.

 doi:10.20944/preprints202401.2198.v1

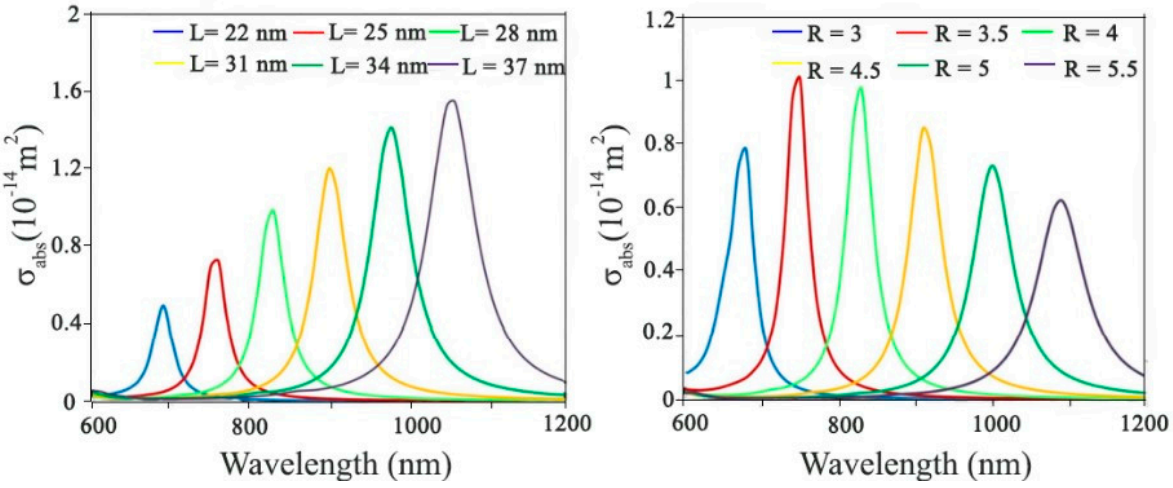

Figure 32. Absorption spectra of nanoframe as a function of different geometric parameters (A) Absorption spectra vs L (W=7nm) (B) absorption spectra vs. R=L/W (L=28nm).

4.4. Industrial Applications (Dye removal)

4.4.1. Methyl Red

Metal nanoframes have been used in the past for the detection of dyes [94]. UV-Visible absorption spectra showed that MR+Ag/Au Fr5 possesses more intense peak absorption peaks at 415,508,650 nm (Figure 33A). By analyzing the SERS spectra of Ag/Au NFs, the absorption peak intensity of these NFs was found to be more intense as compared to silver nanoplate structure. It is just because of the efficient active surfaces on the nanoframe structure due to intense edges and vertices which in turn hold the responsibility of enhanced resonance signal. Ethanol-diluted methyl red dye was excited by a laser signal of 532 nm. This NF material served as the best SERS podium to detect methyl red dye as it was found to be stable, and reproducible with a high enhancement factor and low limit of detection (10^{-5}) as compared to its nanoplate structure. SERS spectra showed that Ag/Au Fr5 sample possesses a precise and distinct SERS signal (Figure 33B). The RSD (relative standard deviation) value for the SERS signal at 1613 $cm^{-1}$was found to be 2.3% which depicts the superb reproducibility of NFs.In comparison to methylene blue, rhodamine 6G the SERS signal intensity for methyl red was stronger and more intense.

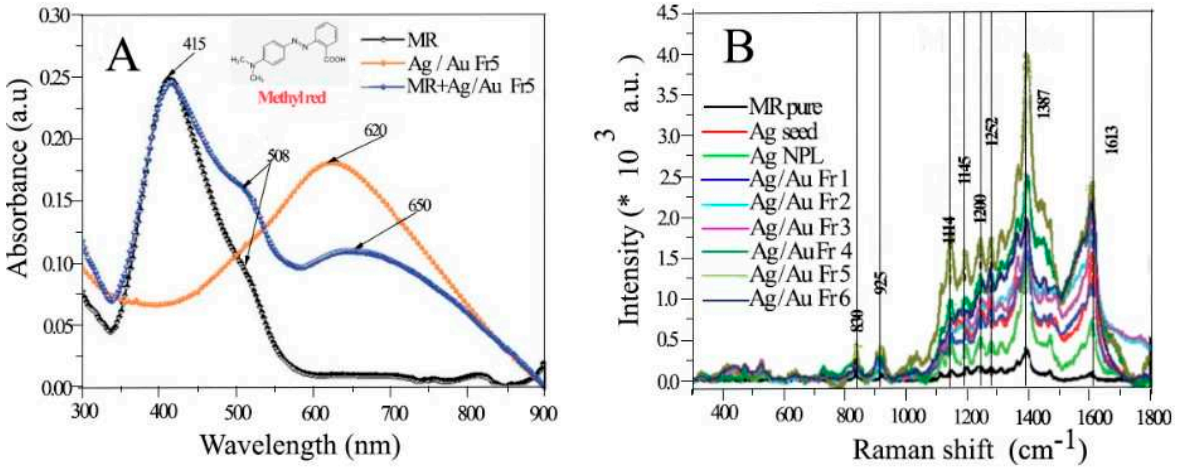

Figure 33. (A) UV-Visible absorption spectra of MR, Ag/Au Fr5, MR+Ag/Au Fr5 at 10^{-5} M concentration of MR (B) SERS spectra of 10^{-5} M methyl red on Ag/Au nanoframe substrate.

 doi:10.20944/preprints202401.2198.v1

4.4.2. Methylene Blue

Photo-electro Fenton electro catalysts like concave octopus-like Pt-Cu nanoframe (COPC-Nfs) have been reported for better wastewater treatment to eliminate dyes [95]. In comparison to previous Fenton processes reported, the photo-electro Fenton method has shown better results due to the self-production of hydrogen peroxide [95] and also due to copper instead of iron used in the Fenton catalyst which depicts enhanced efficiency in a neutral environment. Fenton's degradation can be enhanced by considering NIR signals. [96,97] Methylene blue was used as a sample dye. The degradation performance of these COPC-Nfs and the previously reported photocatalysts were compared and the former was found to be the best one. As far as durability is concerned, after 10 cycles of reuse, they have still shown excellent activity of about 95% (Figure 34A). when treated with 10mA DC, additional electro catalytic activity for H_2O_2 generation was observed (Figure 34B)

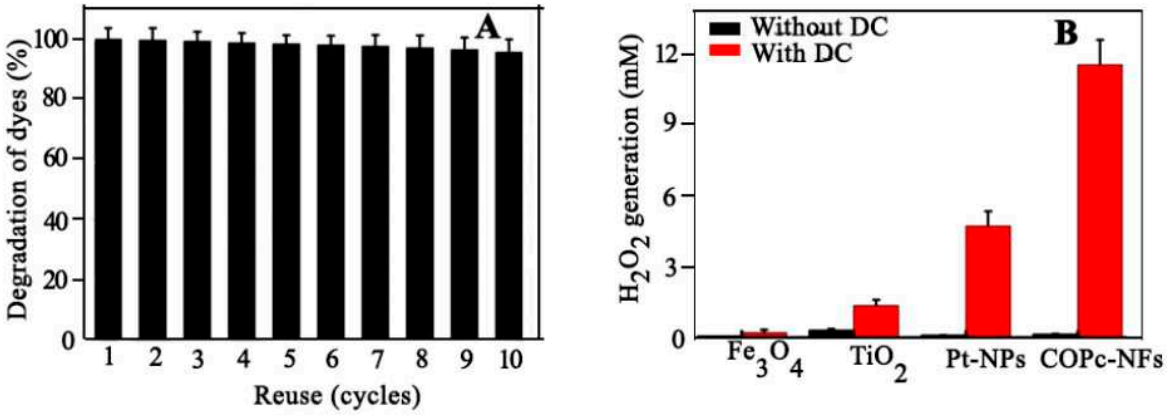

Figure 34. (A) Recyclability of CoPC-NFs treated with DC and NIR-Laser for methylene blue removal within 10 cycles (B) H2O2 generation profile for different Nanocatalysts under DC treatment.

Photo-degradation of MB dye with different Nanocatalysts

Catalyst	Catalyst (g/L)	Irradiation Time (min)	Wavelength (nm)	Degradation %	References
MnFe2O4	0.3	120	Visible	15.1	[98]
MgFe2O4	0.6	180	400-700nm	26.0	[99]
ZnFe2O4	0.6	360	400-700nm	32.0	[99]
CaFe2O4	1.0	360	›420nm	28.0	[100]
BaFe12O19	1.0	360	420-700nm	26.0	[101]
COPC-NFs	0.3	30	808nm	43.9	Present work

Photo-electrode gradation of MB dye with different nanocatalyst

Catalyst	DC power (W)	Time (min)	Degradation (%)	References
TiO2	500	180	22.4	[102]
CO/TiO2	500	120	74.2	[102]
COPC-NFs	500	30	99.2	Present work

4.4.3. 4-Nitro Phenol

AuAgPd polyhedral nanoframe have been reported for their efficient catalytic reduction of 4-nitrophenol in the presence of UV-visible light [103]. The catalytic reduction of these NFs is found to be greater than AuAgPd NPs due to the Plasmon-enhancement effect. The rate constant value

 doi:10.20944/preprints202401.2198.v1

determined for the aforementioned reaction was found to be 1.7 times greater in the presence of light as compared to the light-off reaction condition (Figure 35A,B). UV-Visible spectra showed that the absorption peak for nitrophenol obtained at 400nm started to become less intense slowly and gradually depicting its reduction [104]

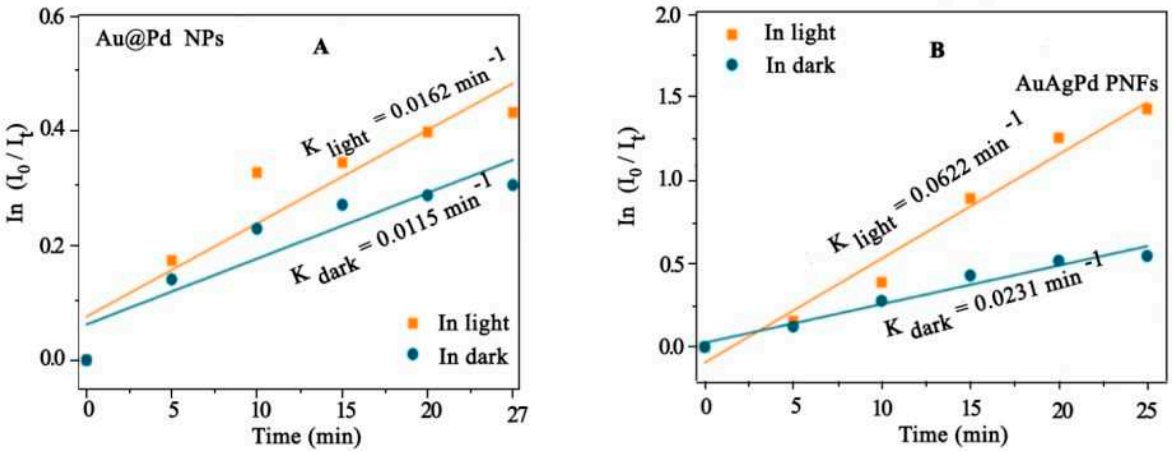

Figure 35. Plots showing ln(I_0/I_t) value versus reaction time under different conditions (A) catalyst Au@Pd NPs (B) AuAgPd PNFs.

4.5. Electro Fenton Application: H2O2 Production in Acids

PdAu-nf has been analyzed as an efficient catalyst for electrochemical generation of H_2O_2 [105] that react with ferrous ions (Fenton's reaction)to produce OH- which is responsible for the rapid degeneration of contaminants, organic. The organic dye rhodamine B (RHB) was used as a sample dye. PdAu-nf causes very fast disintegration of dye in a very short period. UV-Visible analysis showed that almost 90% of Rhb in just the initial 5 minutes of reaction.

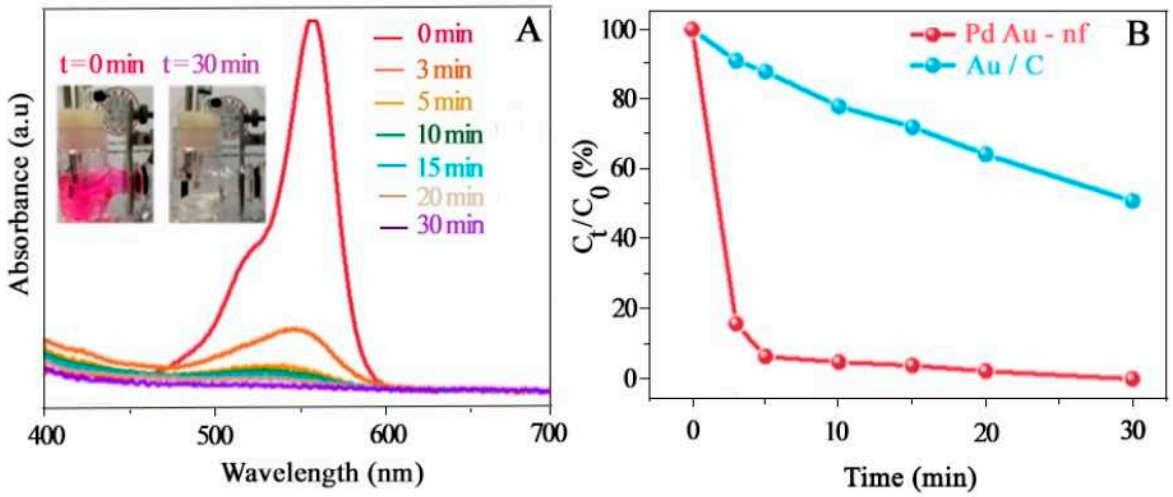

Figure 36. (A) UV-Visible absorption spectra of RhB solution after electro-Fenton reaction at 0.3 V for different times (B) Decay of RhB concentration over time during electro-Fenton reaction at 0.3V by Pd Au-nf and Au/C.

4.6. Electrical Batteries

4.6.1. Lithium-Ion Battery Anodes

Porous manganese tin oxide nanoframe (PMNs) were investigated as the best material for the anode in lithium-ion batteries. They were found to possess excellent durability, capacity, and

 doi:10.20944/preprints202401.2198.v1

reversibility [74]. Different samples were checked for their reaction rates at different current densities like PMNs, bulk $MnSnO_3$, and SnO_2. The one which could produce better capacitance either at low or higher current densities was PMNs anode due to its shorter grain size (Figure 37A).In addition to that, due to their smaller diameter PMNs offer less resistance and as a result, they enhanced interface charge transfer which further augmented their rate properties as compared to bulk MnSnO3. As for as durability is concerned even after 100 cycles PMNs were able to transfer a stable capacity of 912.0 mA h g^{-1} whereas other samples(Bulk $MnSnO_3$, and SnO_2) could only transfer the stable capacity of 383.2 and 223.1 mA h g^{-1} respectively. Due to shorter grain size and porous structure, PMNs samples have shown higher capacities at different voltage ranges. (Figure 37B). (HMBNFs) hierarchical multilayered bipyramid nanoframes made up of ZnO/CoO were also investigated to possess very efficient cycling ability, and better electrochemical performance, [106] when they were analyzed as anodic material for Li-ion batteries.

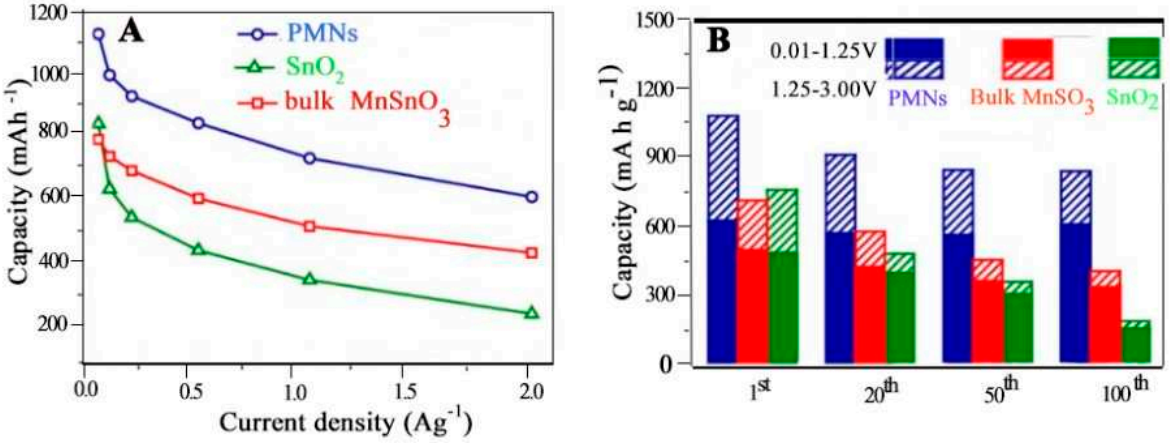

Figure 37. Electrochemical properties PMNs, bulk MnSnO3, and SnO2: (A)_Rate properties at varied current densities (B) capacity variation at two voltage ranges with respect to the cycle number.

4.6.2. Na-Ion Batteries

Na ion batteries (NIBs) are considered to be the best ones in comparison to Li-ion batteries due to their natural reserves and low cost [107,108]. Copper-doped $CoSe_2$ nanoframe cubics (Cu-$CoSe_2$-NFCs) have been reported as the best electrodic materials for NIBs. [109]. The charging capacity of these NFs doped with copper and without copper was found to be 470mAh g^{-1} and 420mAh g^{-1} respectively. The rate performance of Cu-$CoSe_2$-NFCs electrode at different current densities have confirmed their superb specific activity (Figure 38A). The presence of Copper has also increased the electrical conductance of these NFs as depicted by EIS (Figure 38B). Moreover, Cu-$CoSe_2$-NFCs were able to retain 90% charging capacity even after 100 cycles.

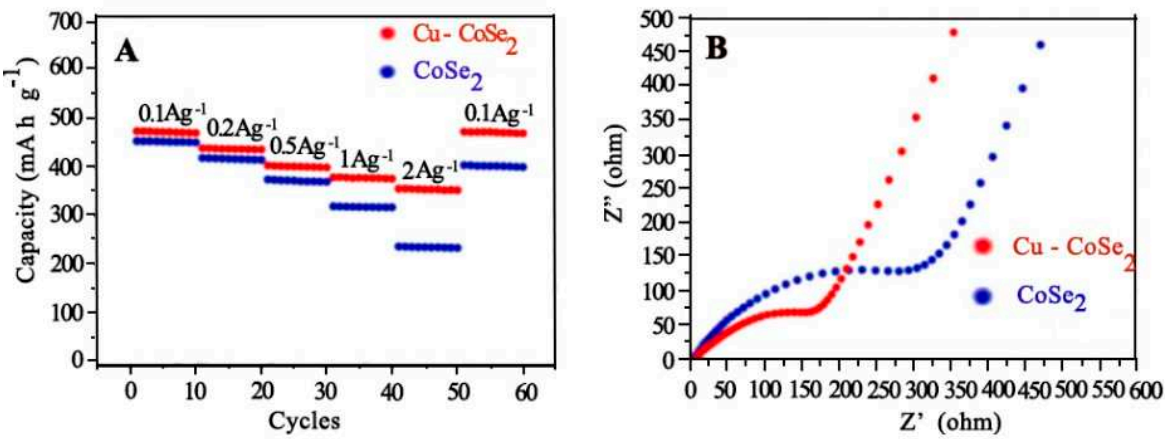

 doi:10.20944/preprints202401.2198.v1

Figure 38. Electrochemical properties of Cu-CoSe2 NFCs (A) Rate property at 0.1-2 Ag-1 (B) Electrochemical impedence spectra.

4.7. Energy Storage Devices

4.7.1. Li-S Cells

Lithium-sulfur pouch cells are considered to be the best energy storage devices due to their high energy density and specific activity [110,111]. 3D Zn Co N codoped carbon NFs (3DZCN-C) are reported as a cathodic material for these cells due to their best activity in inhibiting the shuttling effect of lithium polysulphides (LiPS) with superb cyclability and durability. [112]. Moreover, the discharge capacity of these cells comprising 3DZCN-C reaches up to 975.6 mAh^{-1} at 0.5C, and the decay rate even after 1000 cycles is very low i-e 0.03% (Figure 39). The 3D structure of these nanoframes offers a highly porous structure and the availability of nitrogen vacancies enhances the Li-ion diffusion coefficient thus improving electrochemical properties

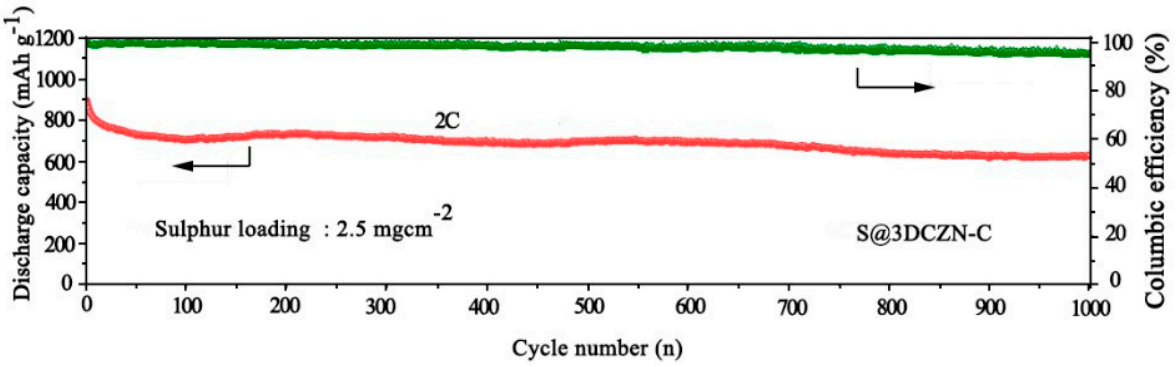

Figure 39. The longlasting cyclic performance of S@ 3DZCN-C at 2C.

4.7.2. Supercapacitor Electrodes

An asymmetric supercapacitor system has been designed by using 3D nanoframes such as sulphurized Ni-Al as a positive electrodic material and (Bi-Ce-S) as a negative electrodic material [113]. Instead of conventional carbon-based negative electrodic material Bi-based material is preferable due to benefit of high capacitance, and easy manufacture. [114,115]The capacitance of sulphurized electrodic material is high i-e 1230.6 F g^{-1} as compared to the material without substitutional Sulphur present i-e 896 Fg^{-1} at a current density of 1A g^{-1} (Figure 40A). The capacitive retention at 20 Ag^{-1} was determined as 69.8% and 59.3% respectively. This electrode was found to possess 81.4%capacitive retention even after 4000 cycles (Figure 40B). Moreover, the specific capacitance of Bi-Ce-S was high as compared to Bi-S when the current was increased from 1 to 10 A g^{-1}. The capacitive retention was 92.2% at a current density of 10 Ag^{-1} for the Bi-Ce-S electrode. The capacitive retention for the whole device was 80.6% at 10 Ag^{-1} with coulombic efficiency of 96.9% even after 8000 cycles (Figure 40C).For device fabrication, the mass ratio of material required for both electrodes was determined through charge-balance theory [116,117].

 doi:10.20944/preprints202401.2198.v1

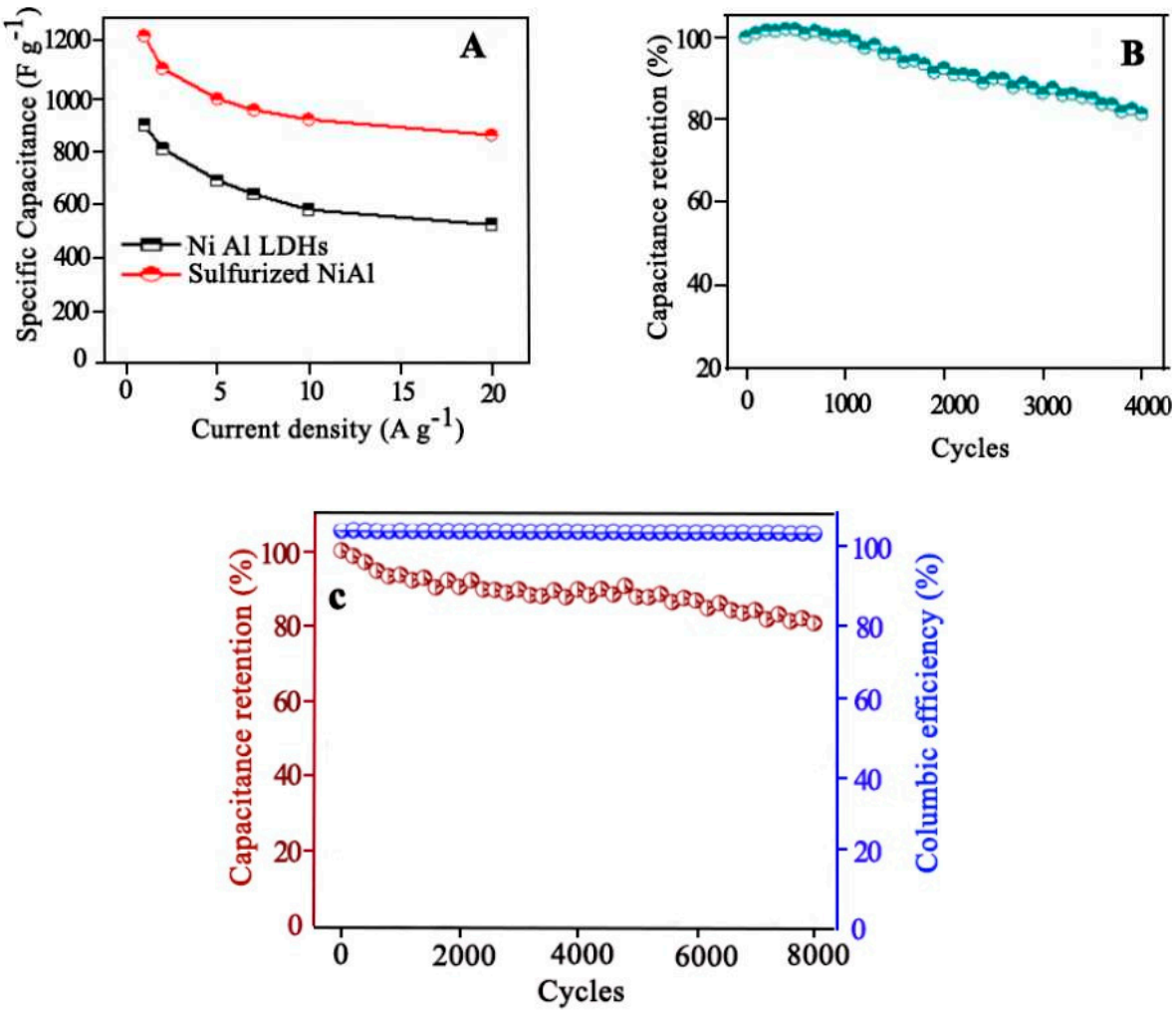

Figure 40. electrochemical performance of (A)Relationship between specific capacitance and current density of sulphurized and Ni-Al LDHs (B) Cyclic performance of sulfurized NiAl at 20 A $g.^{-1}$(C) Cyclic stability and capacitance retention of NiAl//Bi-Ce-S ASC device at 10 Ag-1.

4.8. Surface-Enhanced Resonance Spectroscopy (SERS)

In SERS there is the production of more intensified Raman signals due to the molecules absorbed on the surface and hence analytes with very low concentrations can be detected easily. Some specific sites of these absorbed molecules called "hotspots" are mainly responsible for the enhanced intensity of Raman signals which contribute to the overall intensity factor. The SERS activity of Au nanoframes has been compared with Au nanospheres of the same size [118]. Laser signals of 633nm irradiations were used to detect SERS signals (Figure 41A). It was reported that the Raman signals originating from the substrate surface formulated with Au nanospheres were almost 6 times less intense as compared to Au nanoframes of similar size due to the existence of intramolecular hotspots along with intermolecular ones later (Figure 41B).In another synthetic strategy, a gold ring inside a triangle metal nanoframe was synthesized and this firm structure was found to be suitable for near-field focusing as they were able to withstand high temperature and oxidizing conditions. They have also played their part in the so-called" lightening rod effect" [119]

 doi:10.20944/preprints202401.2198.v1

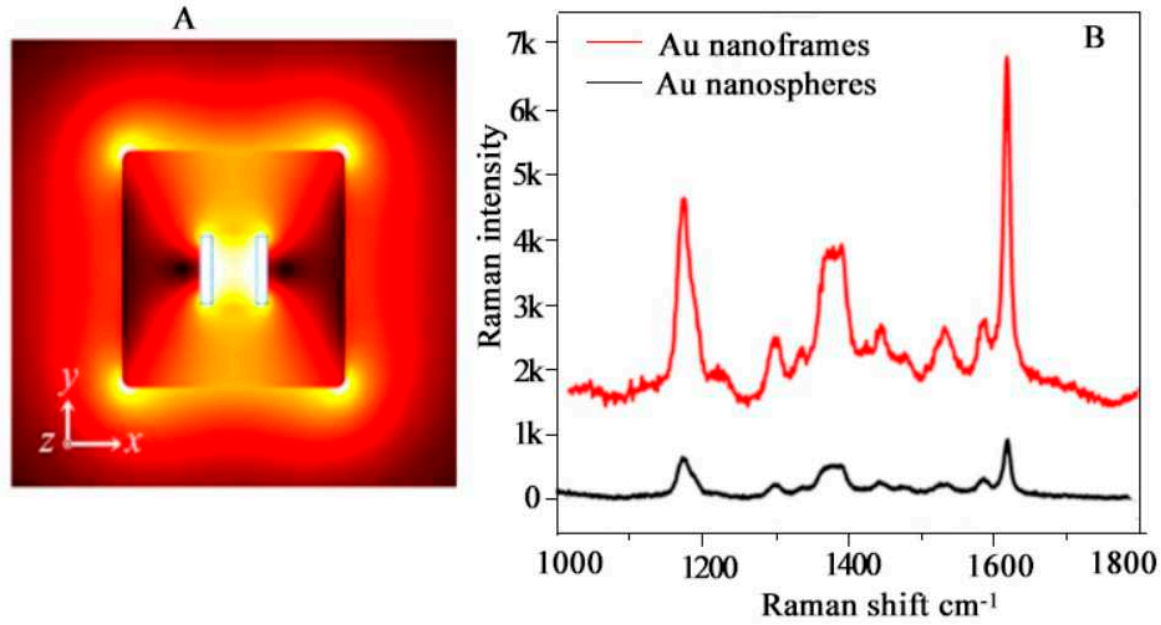

Figure 41. (A) Electric field distribution of Au nanoframe. A laser of 633nm wavelength was irradiated from the z-axis with polarization in the x direction. A dotted square indicates the area of maximum electric field enhancement (B) SERS spectrum of crystal violet (10^{-6} M) absorbed on the substrate modified with Au nanoframe and Au nanosphere.

4.9. Fuel Cell Electrolysis

Pt-Co nanoframes were analyzed for a fabulous performance in fuel cell technology for both MOR and ORR in acidic and alkaline media and also for their structural stability. [120] First of all, electrocatalytic activity for ORR measurement was detected through CV graphs in an acidic medium (Figure 42C) Initially, the ECSA was found to be 50.0 m2 gPt $^{-1,}$ and after 10,000 cycles value reduced only to 45.8 m2 gPt $^{-1}$. It ensured excellent stability and durability of Pt-Co nanoframes in an acidic medium Moreover the specific and mass activity was found to be 0.80 mA cm-2 and 0.40 A mgPt $^{-1}$ie 6 and 4 times greater as compared to Pt/C (Figure 42D). In basic media, CV was performed in the same manner as in an acidic medium to calculate ECSA (Figure 42A). The mass activity left behind after 2000 and 6000 cycles was found to be 0.37 and 0.31 A mgPt $^{-1}$ respectively which is higher than the value for commercial Pt/C (Figure 42B). For MOR activity, CA responses of Pt-Co nanoframes and Pt/C were analyzed at 0.67 VRHE. It was reported that after 1800 cycles the activity of Pt/C declined from 0.31 to 0.02 A mgPt $^{-1}$ which is almost 94% loss but Pt-Co nanoframe suffered only little degradation with the mass activity of 0.33 A mgPt $^{-1}$.CV curves were obtained in

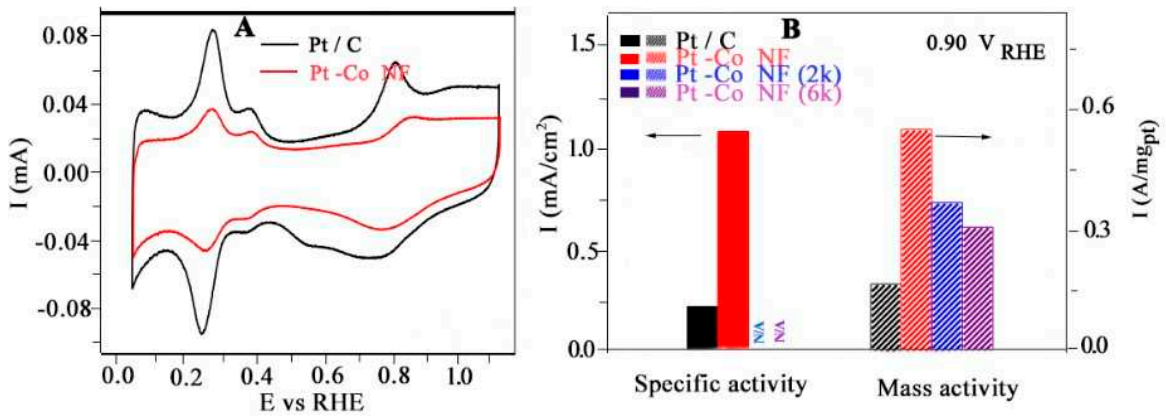

 doi:10.20944/preprints202401.2198.v1

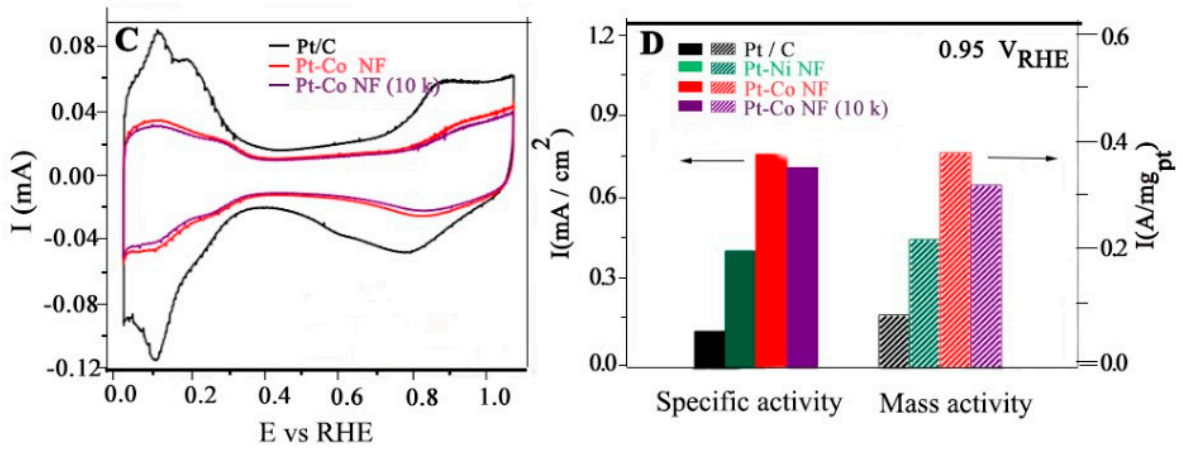

Figure 42. Electrochemical properties of Pt-Co nanoframes (A, B) 1M KOH electrolyte (C.D) 0.1M HClO4 (A,C) CV curves (B,D) specific and mass activity.

4.10. Sensing of Gaseous Molecules

4.10.1. VOCs and CWA (Chemical Warfare Agent)

Sensing of gaseous molecules-Benzenethiol (BT) is an important aspect of explosives, medical diagnostics, and many industrial protocols. [121] SERS spectra of BT were analyzed using 3D Au NF and 3D Au nanoparticles for adsorption of gaseous molecules i-e 10^{-2} M benezethiol. After 60s exposure time, gold nanoframe showed very clear Raman peaks but gold NP gave peaks after an exposure time of 150s. This fast sensing property of Au NF can be used for sensing toxic species like VOCs and CWA (chemical warfare agents). Moreover, for 10^{-14} M benzenethiol molecule, the 3D Au nf arrays show characteristic peaks but Au NP under the same experimental conditions have shown no clear signals. (Figure 43).

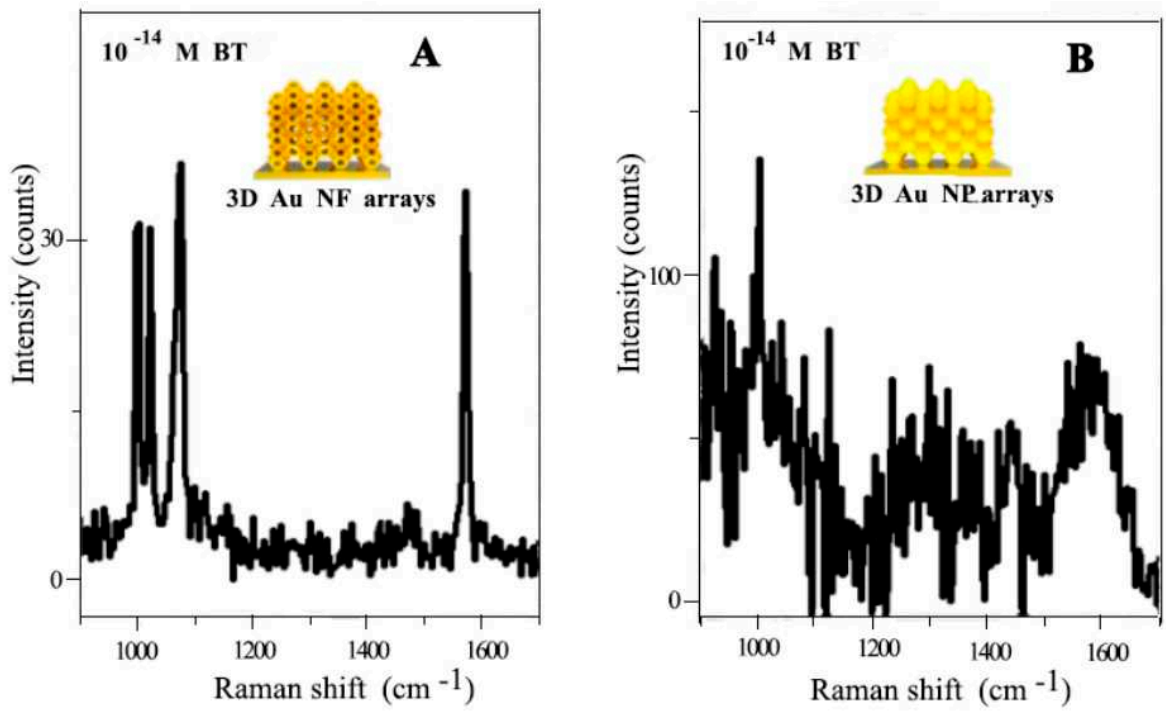

Figure 43. SERS spectra of benzene thiol (10^{-14}) M adsorbed on (A) 3D arrays of Au nanoframe with 18 nm thickness (B) 3D Au nanoparticle arrays.

Preprints.org (www.preprints.org) | NOT PEER-REVIEWED | Posted: 31 January 2024 doi:10.20944/preprints202401.2198.v1

4.10.2. H_2S

Recently it is reported that nanoframes can be used for hydrogen sulfide gas detection. In comparison to solid nanocubes, PdRh SC/ZnO the hollow nanocube PdRh HC/ZnO-based sensors possessed better sensing activity towards H_2S gas showing good selectivity towards H2S gas in comparison to all other gases detected (Figure 44A) [122] It is because the latter has the greater provision of surface area for the gas to adsorb and also due to the hollow structure passage of gas becomes easy and makes redox reaction between gas molecules and adsorbed oxygen anions more feasible. With the increase in temperature the sensing ability of sensors first increases and then decreases due to competition between gas adsorption and desorption. (Figure 44B). Fe-doped MOF-derived porous C-based NFs i-e $Zn_{10}Fe_1$-C-900 have been proposed as efficient H_2S sensing with a fast response time of 0.1 s and recovery time of 0.6 s, long-term stability of up to 8 days, and LOD up to 0.13µg ml^{-1} [123]. With the increase in H_2S concentration, CTL sensor intensity also increases (Figure 45B).

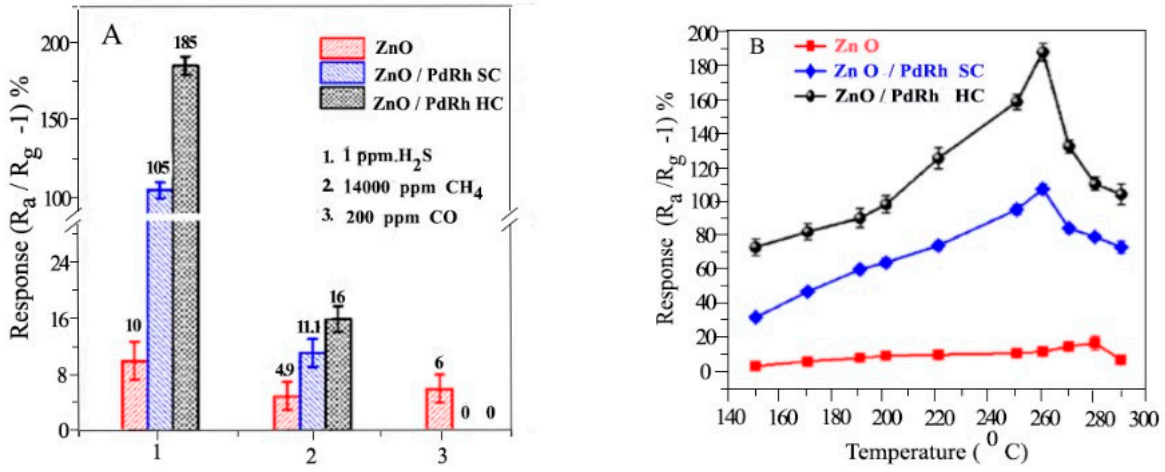

Figure 44. Responses of ZnO, PdRh SC/ZnO, and PdRh HC/ZnO based sensors to(A)1 ppm of H2S, 14 000 ppm of CH4, and 200 ppm of CO at 260 °C (B) 1 ppm of H_2S at varied temperature.

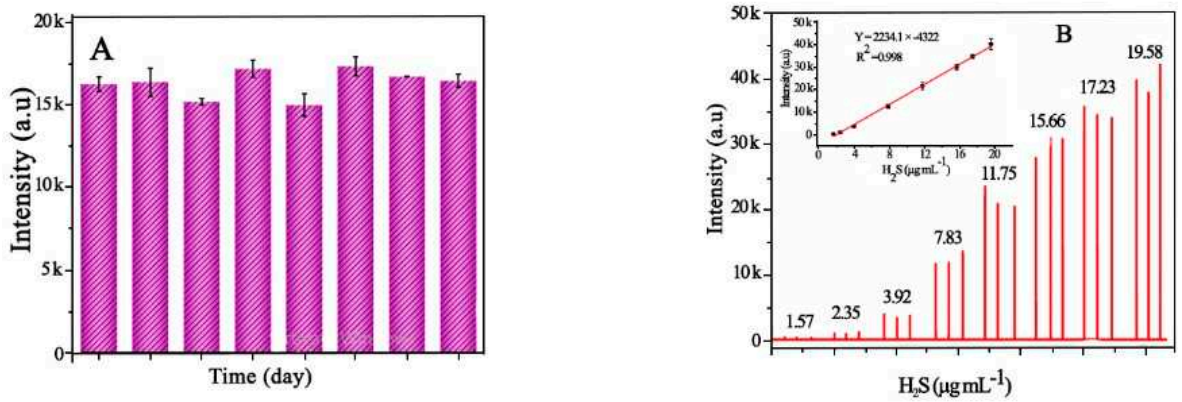

Figure 45. (A) Stability of proposed CTL-based sensor based on $Zn_{10}Fe_1$-C-900 within 8 days (B) CTL sensor response to different H_2S concentrations.

 doi:10.20944/preprints202401.2198.v1

Comparison of different H_2S CTL gas sensors

Sensing materials		Temperature (°C)	Response/recovery time	LOD	References
Metal free	BN	245	0.1/0.2 s	0.52µgmL-1	[124]
	F-SiC	298	0.6/1.0	3ppm	[125]
Metal oxide	Fe2O3	320	15/120	3ppm	[126]
	MnO2	224	0.3/0.4	0.28µgmL-1	[127]
Metal-Carbon complex	Mn3O4/g-C3N4	184	0.6/0.6	0.13µgml-1	[128]
	Fe2O3/g-C3N4	183	0.1/0.6	0.5µgmL-1	[129]
Metal-doped porous carbon nanomaterial	Fe doped Porous carbon	215	0.1/0.6	0.13µGmL-1	Present work

4.11. Reduction of CO_2

4.11.1. Photocatalytic

The main products after the photocatalytic reduction of CO_2 are CO and H_2. Photocatalytic reduction of different sample materials like ZFs [130]. (ZrO_2 nanoframe, ZFs-TCCP (Tetrakis-4-carboxyphenyl porphyrin), HNTM (bulky zirconium porphyrin-based metal-organic framework), and then the one with the best activity was checked with different concentrations also. It was concluded that ZFs-TCPP-Ni showed the highest CO evolution yield among all other samples with 6mg the optimum amount of catalyst used (Figure 46A,B). Moreover, no activity drop of ZFs-TCPP-Ni was found during recycling tests ensuring its excellent stability as well (Figure 46D) EIS plots showed its reduced charge transfer resistance under light irradiation(Figure 46C).

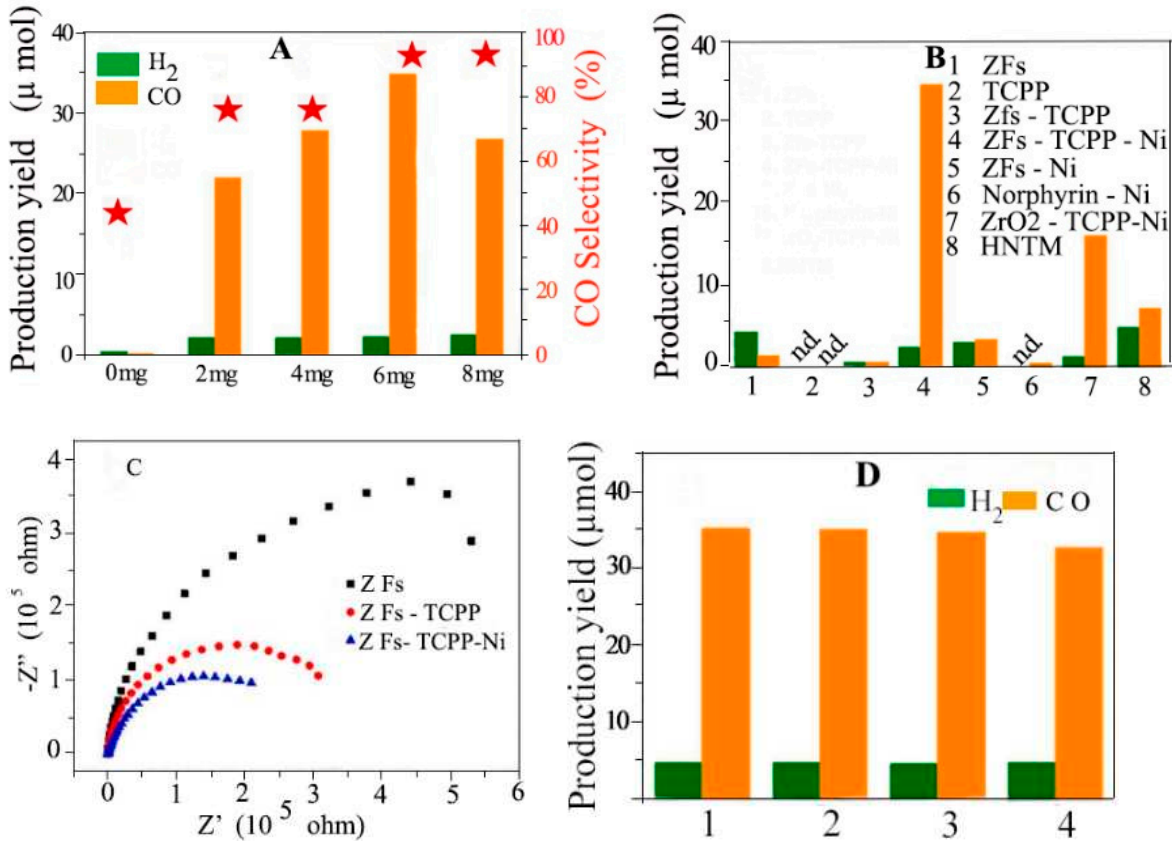

Figure 46. Photocatalytic performance of ZFs-TCPP-Ni (A) varied amount (B) Different samples(C) EIS plots (D) Cyclic stability.

 doi:10.20944/preprints202401.2198.v1

4.11.2. Electro Catalytic

In addition to having excellent catalytic performance towards ORR FeSAs/CNF-900 (C-based MOF has been used by some researchers for electro catalytic reduction of CO2 [131] LSV Curve depicts low over potential losses for CO_2 reduction and the value of onset potential measured is positive. The current density and TOF value found for this catalyst for CO production showed high value among all other catalysts ie 86.9% at 0.47V and 639.9h^{-1} among all other sample catalysts used (Figure 47A).Moreover, by increasing the pyrolysis temperature selectivity of CO product increases (Figure 47B).

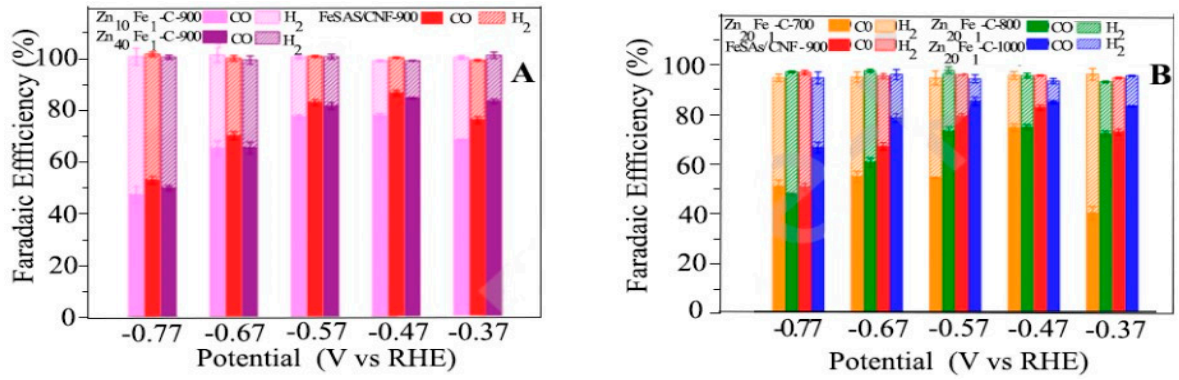

Figure 47. Faradaic efficiency for production of CO and H2 depending on potential (A) ZnxFey-C-900 (B) $Zn_{20}Fe_1$-C-T catalysts.

4.12. Hydrogen Enrichment and Molecular Sieving

The hydrogenation reaction is an elementary constituent in metal catalysis. How efficiently this reaction will proceed, depends upon the use of the most suitable metal surface for absorption as well as dissociation of hydrogen on that surface. The H_2 adsorption efficiency for three different catalysts was compared i-e Pt-Ni polyhedral, Pt-Ni frame, and Pt-Ni frame @ MOF, and the best performance among all of them was founded for the last one (Figure 48A) [50].An important hydrogenation reaction of 1-chloro-2-nitrobenzene to form 2-chhloroaniline, was used as a test reaction to check the adsorption capability of catalyst which shows that Pt-Ni frame @ MOF possesses greater %yield for 2-chloroaniline (Figure 48B).

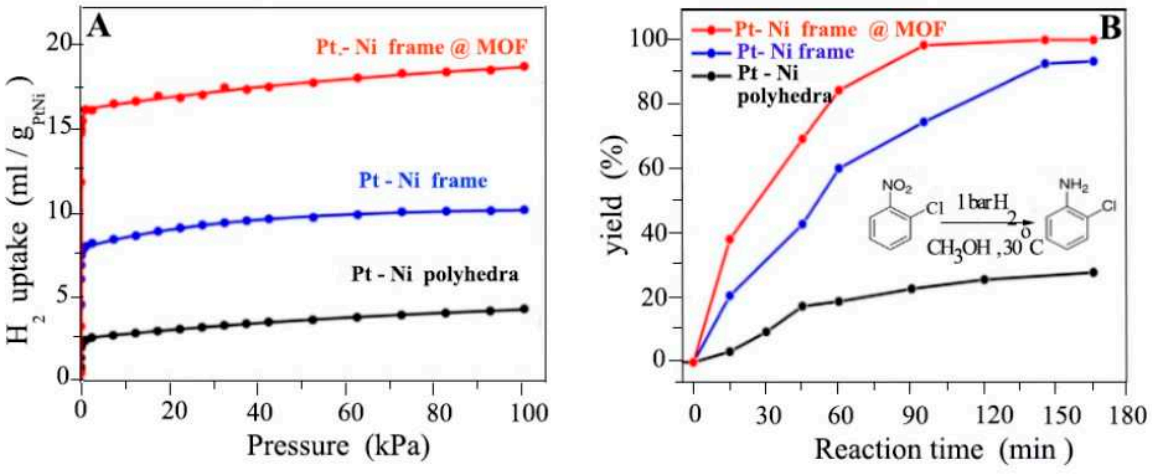

Figure 48. Catalytic hydrogen efficiencies of Pt–Ni polyhedra, Pt–Ni frame, and Pt–Ni frame @ MOF. (A) Comparison of H2 adsorption isotherm at 273 K, 1bar among three different catalysts (B) % yield of 2-chloroaniline produced as a result of hydrogenation of 1-chloro-2-nitrobenzene.

 doi:10.20944/preprints202401.2198.v1

4.13. Spectator of Co^{+2} Ions

GSH-Ag/Au Nfs (gluthione) modified nanoframes are reported as a best candidate to detect Co+2 ion [132]. UV-Vis spectrophotometry showed that there exists a linear relation between the absorption intensity of peaks with increasing concentration of Co^{+2} ions (Figure 49B). Therefore, these NFs can be used for quantitative analysis of cobalt ions up to 1.7 micromolar. GSH-Au/AgNF have shown high selective detection of Co^{+2} ion among all other ions (Figure 49A).

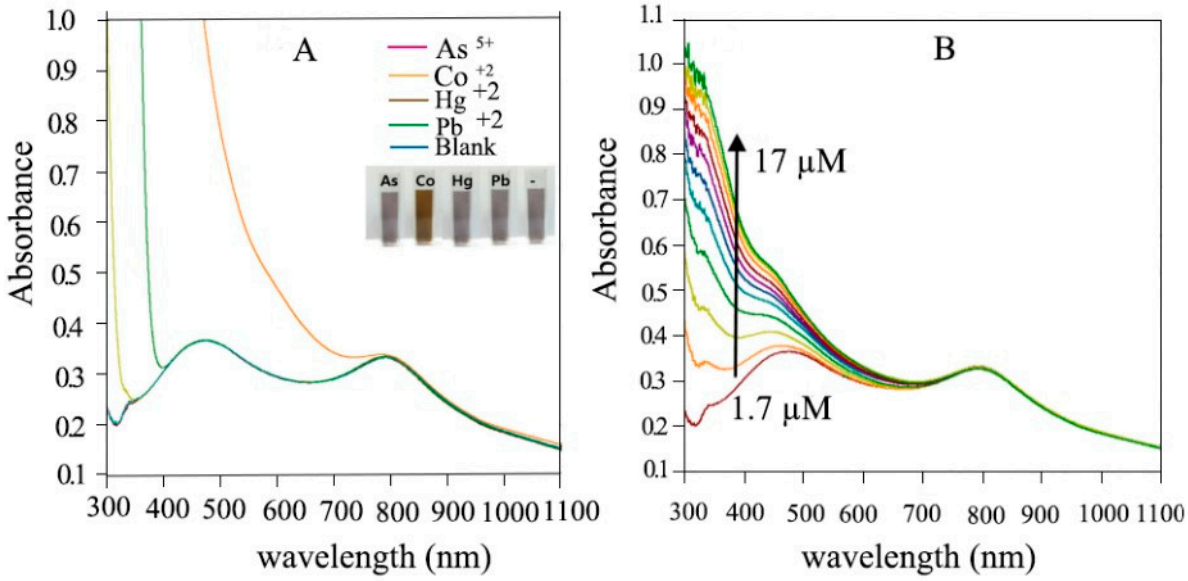

Figure 49. UV-Visible spectra of GSH-Ag/Au nanoframes (A) for different metal ions (B) various concentration of $Co^{+2.}$

4.14. Biomass Upgrading

Metal nanoframes can be used as a catalyst for biomass upgrading. To investigate the catalytic activity of ZrO_2-promoted Ni (Ni/ZrO_2) catalysts, biomass acids like octanoic (OA,C8) and stearic acids(SA,C18) were used [133] The catalyst used was in various forms like Ni/ZrO_2-F (nanoframe), Ni/ZrO_2-H (hollow sphere), Ni/ZrO_2-C (commercial NPs). Among all of them, Ni/ZrO_2-F was found to be a more suitable and excellent catalyst in the conversion of OA and SA due to its high turn-over frequency of 10.2 and 3.4 h^{-1} respectively as compared to Ni/ZrO_2-H and Ni/ZrO_2-C (Figure 50). Their turnover frequency was found to be 8.8 and 2.7 h^{-1} and 5.5 and 1.6 h^{-1} respectively.

catalyst	Conversion %	Yield %			
		Heptane	Octane	octanol	others
NiZrO2-C	54.2	38.7	6.6	3.2	5.6
NiZrO2-H	86.4	70.3	6.9	2.6	6.3
NiZrO2-F	100.0	86.0	6.0	2.1	2.1

Reaction conditions:
Octanoic acid (1g), decane (100mL), catalyst (0.1g), 330^{0}C, 3MPa, H2, 4h

Catalyst	Conversion %	Yield %			
		Heptane	Octane	Octanol	Others
NiZrO2-C	48.1	38.6	5.8	1.5	2.2
NiZrO2-H	80.3	69.5	7.8	1.3	1.7
NiZrO2-F	100.0	89.3	7.1	1.2	2.4

Reaction conditions:

 doi:10.20944/preprints202401.2198.v1

Stearic acid (1g), Dodecane (100Ml, catalyst (0.1 g), 260^{0}C, 3MPa, H2,

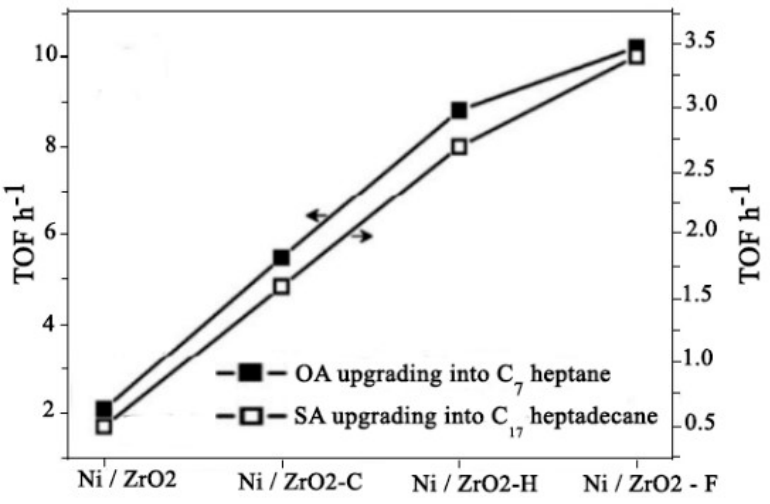

Figure 50. TOF values for Ni/ZrO$_2$-F, Ni/ZrO$_2$-H, Ni/ZrO$_2$-C,Ni /ZrO$_2$.

4.15. Antibacterial Performance

AgAuYSCNFs (AgAu-yolk shell cubic nanoframes) have been analyzed as an efficient material for antibacterial activity by using *staphylococcus aureus (*MRSA) as a testing bacteria. When no laser irradiations were used, huge amounts of bacteria were found on the plate in the absence of these yolk-shell nanoframes. [134]However, by increasing the concentration of AgAuYSCNFs, the antibacterial efficiency was also increased (Figure 51A). Moreover, with increase in temperature photothermal performance was increased. (Figure 51B). The YSCNF-60 was found to possess good photothermal activity with increasing temperature (Figure 51C). The antibacterial activity of these nanoframes was further escalated when irradiated with NIR for just 10 mins due to the synergistic effect of Ag present and the high temperature produced as a result of photothermal conversion. They possess excellent photothermal stability even after 5 Laser irradiation ON/OFF cycles (Figure 51D).

There is a need to make conventional GNPs more tolerant towards high temperatures, reductants, and surfactants. [135]Catechin related to tea polyphenol has been reported as a green reducing agent to synthesize gold NPS and also make the chelation of metal ions easier. Thus sample named pGNP-Fe composite can generate a large amount of intracellular ROS in situ which in turn makes the antibacterial effect last for a greater period. [136]

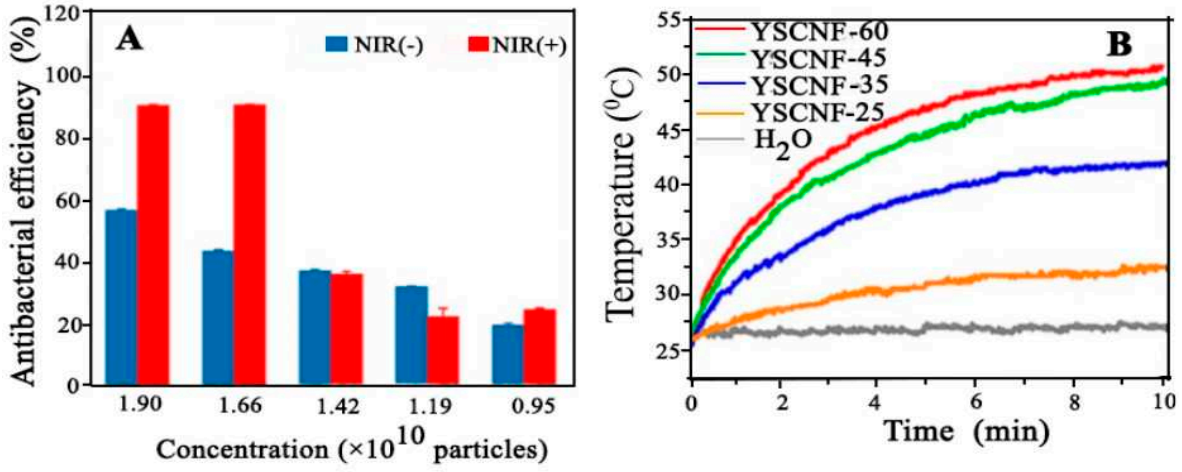

 doi:10.20944/preprints202401.2198.v1

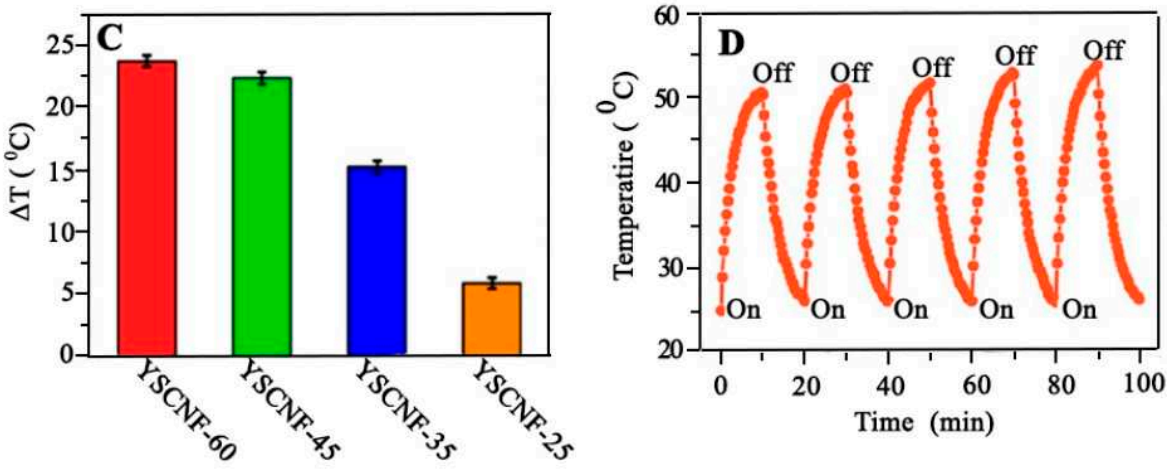

Figure 51. (A) growth retardation of MRSA and antibacterial activity at different concentrations of AuAg YSCNFs-60 with and without NIR radiation (B) Photothermal conversion performance of pure water and YSCNFs recorded with NIR laser (808nm).(C) temperature changes for YSCNFs with different edge length (D) Photothermal stability of YSCNF-60 with five cycles of ON/OFF laser irradiation.

4.16. Nano Probes for Bio Sensing

4.16.1. HCG

It is reported that 3D Au dual rim NFs showed greater bio sensitivity towards HCG (human chorionic gonadotrophin) as compared to their 2D structure due to Surface-enhanced Raman scattering which in turn is due to many intra-nanogaps present in 3D structure (Figure 52) [137]. An intense electric field can be produced due to the well-known "lightening rod effect" [138].

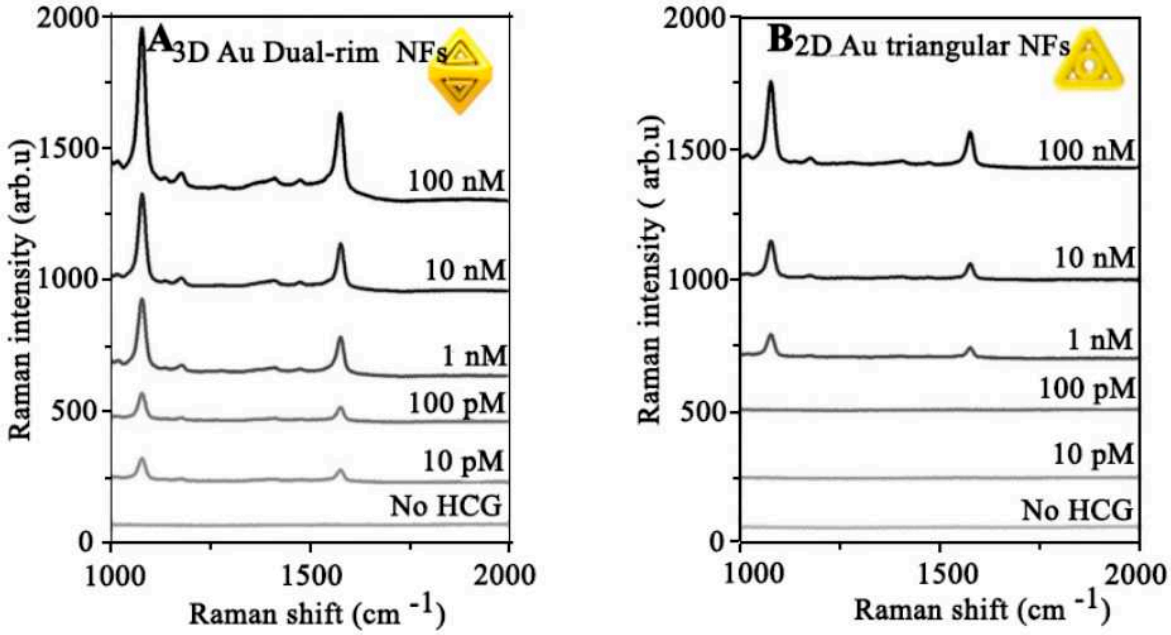

Figure 52. SERS-based detection of HCG hormone (A) 3D Au dual-rim NFs and (B) 2D Au triangular dual-rim NFs with different concentrations of HCG.

 doi:10.20944/preprints202401.2198.v1

4.16.2. Glucose in Human Tears

Despite electrochemical [139]and photochemical [140] biosensors as the best and most efficient sensing tools, PEC(photo-electrochemical) is the most efficient biosensing strategy comparatively, showing both the advantage of photochemical and electrochemical bio sensing. [141,142]. NIR-PEC biosensors have been designed by using h-BN/Au_5Pt_9 nanoframes as electrodic material for monitoring of glucose in human tears with detection limit of upto 0.406 nM. [143] DPV curves have shown that oxidation current increases with increasing glucose concentration(Figure 53A) These NFs offered better results as compared to the previously reported results using electro-catalytic and visible light reactions. [144–146]. As far as stability is concerned, this NIR-PEC biosensor was able to maintain 96.7% of the current of its initial value even after 20 days. The RSD for an amperometric current response was found to be not more than 5%. The glucose level in tears and blood was found to be increased using h-BN/Au_5Pt_9 nanoframes-based NIR-PEC biosensor (Figure 53B)

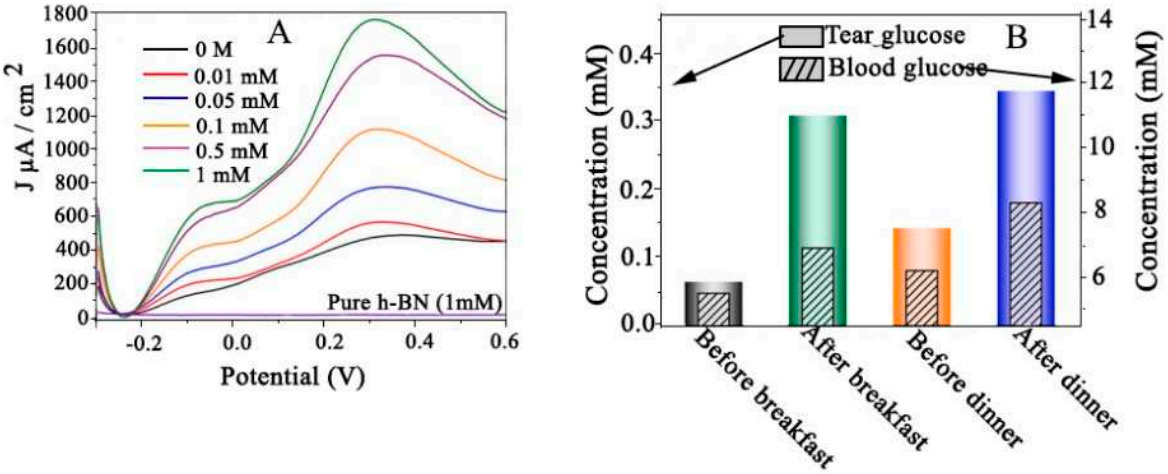

Figure 53. (A) DPV curves of_h-BN/Au_5Pt_9 nanoframes in dark containing different concentration glucose in artificial tears (B) Glucose concentration in tears and blood of volunteer before and after breakfast.

4.17. Hydrogen Production

Due to the expeditious usage of naturally existing energy resources, and their significant role in boosting environmental pollution, there is a need for some clean and renewable energy resources [147]Hydrogen is the best specie to store energy as compared to conventional energy resources like fossil fuel [148].

4.17.1. Photothermal Catalytic

Multishell NFs like 3D C@TiO_2 can be used for the production of hydrogen from waste water containing dyes [149].C@TiO_2 MNF has shown catalytic performance 4.3 times higher than TiO_2 MNF in terms of hydrogen evolution i-e 503 μmolg-$1h^{-1}$ and 116μmolg^{-1} h^{-1} respectively. It was also confirmed that the catalytic activity of C@TiO_2 MNF for hydrogen evolution reaction in the case of pure water was reduced to 35% as compared to rhodamine B-containing water.

4.17.2. Solar-Driven H2 Production

To tackle the emerging issue of energy crises, hydrogen can be produced from water using solar energy [150–152].ZnS nanoframes with 1% doping of copper are reported for their superb photocatalytic activity in terms of hydrogen production in the presence of solar radiation (Figure 54A) [153]. There was no significant decrease in the activity of the catalyst observed even after 5 runs (Figure 54B).

 doi:10.20944/preprints202401.2198.v1

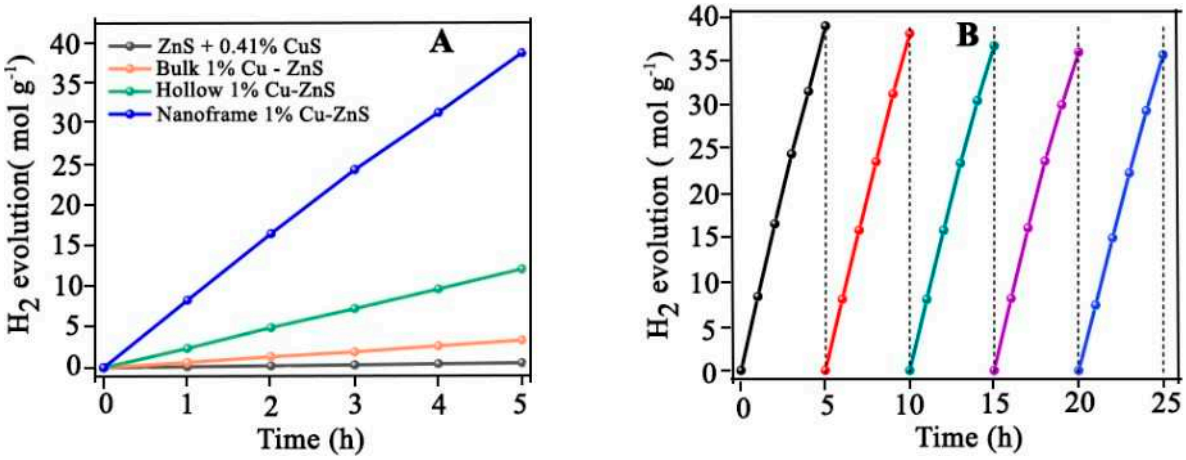

Figure 54. (A) Photocatalytic Hydrogen Evolution curves for x% Cu-ZnS nanoframe (B) Photocatalytic hydrogen production in 5 consecutive cycles for 1%Cu-ZnS nanoframe under solar irradiation.

5. Conclusions

We have briefly discussed the synthesis of nanoframes by different methods. Some methods are most commonly used methods like galvanic replacement reaction, one-pot sysynthesis and chemical etching. However, many other strategies have been used recently by many research groups. nanoframes of three different categories are also discussed depending upon whether they are made of pure single metal, alloys, or some other metal that is present as a dopant in the parent metallic nanoframe structure.in addition to that, many applications of nanoframes have also been overviewed in various fields other than just only in the catalytic domain. These include theranostic, biomedical, sensing or detection of different material, photocatalytic and electrocatalytic reduction of CO2. Apart from having such a unique 3D structure, the unparallel physiochemical properties of nanoframes still pose some serious challenges which need to be addressed in future work-e controlling their thickness, the final product obtained in a very small amount is insufficient to meet industrial demands.

6. Future Directions

Despite having unique physiochemical properties, and spatial 3D structure, challenges still exist in controlling the thickness of ridges, the extent of excavation, and their elemental composition. We can say that the grave concern of future work should be,

- The thickness of ridges can be controlled by tunning the breadth of the metal being deposited on the template surface which in turn can be achieved by the adjustment of the relative amount of both.
- Till now production of NFs is just limited to a very small scale i-e milligrams. Attention should be given in future work to enhance their production to meet industrial demands

References

1. Lee, K.Y., et al., *Novel surfactant-free multi-branched gold stars characterized by inverse photocurrent.* Journal of Materials Chemistry A, 2013. **1**(44): p. 13890-13895. https://doi.org/10.1039/c3ta11983a
2. Liu, X. and D. Astruc, From galvanic to anti-galvanic synthesis of bimetallic nanoparticles and applications in catalysis, sensing, and materials science. Advanced Materials, 2017. **29**(16): p. 1605305. https://doi.org/10.1002/adma.201605305
3. Ridelman, Y., et al., *Metallic nanobowls by galvanic replacement reaction on heterodimeric nanoparticles.* Small, 2012. **8**(5): p. 654-660. https://doi.org/10.1002/smll.201101882 **DOI**: 10.1039/x0xx00000x
4. Collins, G., E. McCarty, and J.D. Holmes, Controlling alloy formation and optical properties by galvanic replacement of sub-20 nm silver nanoparticles in organic media. CrystEngComm, 2015. **17**(36): p. 6999-7005. https://doi.org/10.1039/x0xx00000x
5. Yamamoto, Y., et al., Formation mechanism of plasmonic silver nanohexagonal particles made by galvanic displacement reaction. RSC advances, 2016. **6**(37): p. 31454-31461. https://doi.org/10.1039/x0xx00000x

6. Hangarter, C.M., et al., *Nanopeapods by galvanic displacement reaction.* Angewandte Chemie International Edition, 2010. **49**(39): p. 7081-7085. https://doi.org/10.1002/anie.201001559
7. Parisi, J., L. Su, and Y. Lei, In situ synthesis of silver nanoparticle decorated vertical nanowalls in a microfluidic device for ultrasensitive in-channel SERS sensing. Lab on a Chip, 2013. **13**(8): p. 1501-1508. https://**doi**.org/10.1039/C3LC41249K
8. Mohl, M., et al., *Formation of CuPd and CuPt bimetallic nanotubes by galvanic replacement reaction.* The Journal of Physical Chemistry C, 2011. **115**(19): p. 9403-9409. https://doi.org/10.1021/jp112128g
9. Liu, J., et al., *Fabrication of DNA-templated Te and Bi2Te3 nanowires by galvanic displacement.* Langmuir, 2013. **29**(35): p. 11176-11184. dx.**doi**.org/10.1021/la402678j
10. Mohl, M., et al., *Synthesis of catalytic porous metallic nanorods by galvanic exchange reaction.* The Journal of Physical Chemistry C, 2010. **114**(1): p. 389-393.. https://doi.org/10.1021/jp9083508
11. Tan, Y.-N., et al., Mechanistic Study on the Bis(p-sulfonatophenyl)phenylphosphine Synthesis of Monometallic Pt Hollow Nanoboxes Using Ag*−Pt Core−Shell Nanocubes as Sacrificial Templates. The Journal of Physical Chemistry C, 2007. **111**(38): p. 14084-14090. https://doi.org/10.1021/jp0741049
12. He, P., X.Y. Yu, and X.W. Lou, *Carbon-incorporated nickel–cobalt mixed metal phosphide nanoboxes with enhanced electrocatalytic activity for oxygen evolution.* Angewandte Chemie International Edition, 2017. **56**(14): p. 3897-3900. https://doi.org/10.1002/anie.201612635
13. Wang, C., et al., Nanoboxes endow non-noble-metal-based electrocatalysts with high efficiency for overall water splitting. Journal of Materials Chemistry A, 2021. **9**(2): p. 857-874. https://doi.org/10.1039/x0xx00000x.
14. Cheng, X., et al., *Bimetallic metal-organic frameworks nanocages as multi-functional fillers for water-selective membranes.* Journal of Membrane Science, 2018. **545**: p. 19-28. https://doi.org/10.1016/j.memsci.2017.09.056
15. Xu, Y., et al., Synthesis of bimetallic NixCo1-xP hollow nanocages from metal-organic frameworks for high performance hybrid supercapacitors. Electrochimica Acta, 2018. **285**: p. 192-201. https://doi.org/10.1016/j.electacta.2018.07.211
16. Huang, M., et al., *MOF-derived bi-metal embedded N-doped carbon polyhedral nanocages with enhanced lithium storage.* Journal of Materials Chemistry A, 2017. **5**(1): p. 266-274. https://doi.org/10.1039/c6ta09030c
17. Zhu, J., et al., *Enlarge the biologic coating-induced absorbance enhancement of Au-Ag bimetallic nanoshells by tuning the metal composition.* Spectrochimica Acta Part A: Molecular and Biomolecular Spectroscopy, 2018. **189**: p. 571-577. https://**doi**.org/10.1016/j.saa.2017.08.064
18. Rodrigues, T.S., et al., *Probing the catalytic activity of bimetallic versus trimetallic nanoshells.* Journal of Materials Science, 2015. **50**(16): p. 5620-5629. https://doi.org/10.1007/s10853-015-9114-x
19. Kisukuri, C.M., et al., *Bimetallic Nanoshells as Platforms for Metallo-and Biometallo-Catalytic Applications.* ChemCatChem, 2016. **8**(1): p. 171-179. https://doi.org/10.1002/cctc.201500812
20. Godinez-Salomon, F., et al., Bimetallic two-dimensional nanoframes: high activity acidic bifunctional oxygen reduction and evolution electrocatalysts. ACS Applied Energy Materials, 2020. **3**(3): p. 2404-2421. https://doi.org/10.1021/acsaem.9b02051
21. Li, J., X. Sun, and D. Qin, *Ag-Enriched Ag-Pd Bimetallic Nanoframes and Their Catalytic Properties.* ChemNanoMat, 2016. **2**(6): p. 494-499. https://doi.org/10.1002/cnma.201600080
22. Cheng, D., et al., Simulating Synthesis of Metal Nanorods, Nanoplates, and Nanoframes by Self-Assembly of Nanoparticle Building Blocks. The Journal of Physical Chemistry C, 2009. **113**(10): p. 3986-3997. https://doi.org/10.1021/jp809628w
23. Fang, Z., et al., *Rational design of metal nanoframes for catalysis and plasmonics.* Small, 2015. **11**(22): p. 2593-2605. https://doi.org/10.1002/smll.201402799
24. Xie, S., et al., Synthesis of Pd-Rh core–frame concave nanocubes and their conversion to Rh cubic nanoframes by selective etching of the Pd cores. Angewandte Chemie International Edition, 2012. **51**(41): p. 10266-10270. https://doi.org/10.1002/anie.201206044
25. Nosheen, F., et al., One-pot fabrication of single-crystalline octahedral Pt–Cu nanoframes and their enhanced electrocatalytic activity. Nanoscale, 2013. **5**(9): p. 3660-3663. https://doi.org/10.1039/c3nr00833a
26. Niu, H.-J., et al., One-pot solvothermal synthesis of three-dimensional hollow PtCu alloyed dodecahedron nanoframes with excellent electrocatalytic performances for hydrogen evolution and oxygen reduction. Journal of colloid and interface science, 2019. **539**: p. 525-532. https://doi.org/10.1016/j.jcis.2018.12.066
27. Kao, C.-R., et al., Insights into Transformation of Icosahedral PdRu Nanocrystals into Lattice-Expanded Nanoframes with Strain Enhancement in Electrochemical Redox Reactions. Chemistry of Materials, 2022. **34**(5): p. 2282-2291. https://doi.org/10.1021/acs.chemmater.1c04093
28. Kim, J., et al., Synthesis and Single-Particle Surface-Enhanced Raman Scattering Study of Plasmonic Tripod Nanoframes with Y-Shaped Hot-Zones. Nano Letters, 2020. **20**(6): p. 4362-4369. https://doi.org/10.1021/acs.nanolett.0c01084
29. Luo, S. and P.K. Shen, Concave Platinum–Copper Octopod Nanoframes Bounded with Multiple High-Index Facets for Efficient Electrooxidation Catalysis. ACS Nano, 2017. **11**(12): p. 11946-11953. https://doi.org/10.1021/acsnano.6b04458

30. Kwon, T., et al., Vertex-reinforced PtCuCo ternary nanoframes as efficient and stable electrocatalysts for the oxygen reduction reaction and the methanol oxidation reaction. Advanced Functional Materials, 2018. **28**(13): p. 1706440. https://doi.org/**10.1002/adfm.201706440**
31. Liu, Y., et al., *Template-assisted synthesis of single-crystalline Mn3O4 nanoframes and hollow octahedra.* Solid state sciences, 2012. **14**(10): p. 1462-1466. https://doi.org/10.1016/j.solidstatesciences.2012.08.014
32. Okazaki, K.-i., et al., Fabrication of nanoframe structures by site-selective assembly of gold nanoparticles on silver cubes in an ionic liquid. Chemistry letters, 2011. **40**(1): p. 84-86. **https://doi.**org/10.1246/cl.2011.84
33. Negondeni, J. and T. Ngwenya, *Synthesizing Pt-Ni/C Nanoframes electrocatalyst using the solvothermal and in-house developed method for PEM fuel cells.* Suid-Afrikaans Tydskrif vir Natuurwetenskap en Tegnologie/South African Journal of Science and Technology, 2021. **40**(1): p. 262-266. https://**doi.**org/10.36303/SATNT.2021cosaami.48
34. Chen, X.-L., et al., Uric acid supported one-pot solvothermal fabrication of rhombic-like Pt35Cu65 hollow nanocages for highly efficient and stable electrocatalysis. Journal of colloid and interface science, 2019. **540**: p. 486-494. https://doi.org/10.1016/j.jcis.2019.01.020
35. Snyder, J., et al., *Oxygen reduction in nanoporous metal–ionic liquid composite electrocatalysts.* Nature materials, 2010. **9**(11): p. 904-907. https://**doi**.org/10.1038/nmat2878
36. Snyder, J., et al., Structure/processing/properties relationships in nanoporous nanoparticles as applied to catalysis of the cathodic oxygen reduction reaction. Journal of the American Chemical Society, 2012. **134**(20): p. 8633-8645. https://**doi**.org/10.1021/ja3019498
37. Chen, C., et al., Highly crystalline multimetallic nanoframes with three-dimensional electrocatalytic surfaces. Science, 2014. **343**(6177): p. 1339-1343. https://doi.org/10.1126/science.1249061
38. Xie, S., et al., *Catalysis on faceted noble-metal nanocrystals: both shape and size matter.* Current Opinion in Chemical Engineering, 2013. **2**(2): p. 142-150. https://doi.org/10.1016/j.coche.2013.02.003
39. Yang, T.-H., et al., *Noble-metal nanoframes and their catalytic applications.* Chemical Reviews, 2020. **121**(2): p. 796-833. https://doi.org/10.1021/acs.chemrev.0c00940
40. Wang, Z., et al., Synthesis of Pd nanoframes by excavating solid nanocrystals for enhanced catalytic properties. ACS nano, 2017. **11**(1): p. 163-170. https://doi.org/10.1021/acsnano.6b06491
41. Han, L., et al., Alloy Cu 3 Pt nanoframes through the structure evolution in Cu-Pt nanoparticles with a core-shell construction. Scientific reports, 2014. **4**(1): p. 1-6. https://**doi**.org/10.1038/srep06414
42. Oh, A., et al., Skeletal octahedral nanoframe with cartesian coordinates via geometrically precise nanoscale phase segregation in a Pt@ Ni core–shell nanocrystal. ACS nano, 2015. **9**(3): p. 2856-2867. https://doi.org/10.1021/nn5068539
43. Yang, T.H., et al., *Surface capping agents and their roles in shape-Controlled synthesis of colloidal metal nanocrystals.* Angewandte Chemie International Edition, 2020. **59**(36): p. 15378-15401. https://**doi**.org/10.1002/anie.201911135
44. Qin, Y., et al., *Fine-Tuning Intrinsic Strain in Penta-Twinned Pt–Cu–Mn Nanoframes Boosts Oxygen Reduction Catalysis.* Advanced Functional Materials, 2020. **30**(11): p. 1910107. https://doi.org/10.1002/adfm.201910107
45. Park, J., et al., Platinum cubic nanoframes with enhanced catalytic activity and durability toward oxygen reduction. ChemSusChem, 2016. **9**(19): p. 2855-2861. https://doi.org/10.1002/cssc.201600984
46. Zhang, L., et al., Platinum-based nanocages with subnanometer-thick walls and well-defined, controllable facets. Science, 2015. **349**(6246): p. 412-416. https://doi.org/10.1002/cssc.201600984
47. Lu, X., et al., Fabrication of cubic nanocages and nanoframes by dealloying Au/Ag alloy nanoboxes with an aqueous etchant based on Fe(NO3)3 or NH4OH. Nano Lett., 2007. **7**(6): p. 1764. https://doi.org/10.1021/nl070838l
48. Yoo, S., et al., *Two-dimensional nanoframes with dual rims.* Nature communications, 2019. **10**(1): p. 1-8. https://**doi**.org/10.1038/s41467-019-13738-6
49. Gilroy, K.D., et al., Shape-controlled synthesis of colloidal metal nanocrystals by replicating the surface atomic structure on the seed. Advanced Materials, 2018. **30**(25): p. 1706312. https://doi.org/10.1002/adma.201706312
50. Li, Z., et al., Platinum–nickel frame within metal-organic framework fabricated in situ for hydrogen enrichment and molecular sieving. Nature communications, 2015. **6**(1): p. 1-8. https://**doi**.org/10.1038/ncomms9248
51. Pei, J., et al., Ir–Cu nanoframes: one-pot synthesis and efficient electrocatalysts for oxygen evolution reaction. Chemical communications, 2016. **52**(19): p. 3793-3796. https://doi.org/10.1039/c0xx00000x
52. Kull, S., et al., *Synthesis of Single-Crystalline Lead Sulfide Nanoframes and Nanorings.* Chemistry of Materials, 2019. **31**(15): p. 5646-5654. https://doi.org/10.1021/acs.chemmater.9b01508
53. Gruzeł, G., et al., Conversion of bimetallic PtNi 3 nanopolyhedra to ternary PtNiSn nanoframes by galvanic replacement reaction. Nanoscale, 2019. **11**(12): p. 5355-5364. https://doi.org/10.1039/x0xx00000x
54. Yang, L., et al., Construction of light-harvesting system for enhanced catalytic performance of Pd nanoframes toward Suzuki coupling reaction. Journal of Materials Chemistry A, 2017. **5**(21): p. 10150-10153. https://doi.org/10.1039/x0xx00000x

55. Ye, H., et al., *Ru nanoframes with an fcc structure and enhanced catalytic properties.* Nano letters, 2016. **16**(4): p. 2812-2817. https://doi.org/10.1021/acs.nanolett.6b00607
56. Ahn, J. and D. Qin, Fabrication of Nanoscale Cage Cubes by Drilling Orthogonal, Intersected Holes through All Six Side Faces of Ag Nanocubes. Chemistry of Materials, 2019. **31**(21): p. 9179-9187. https://doi.org/10.1021/acs.chemmater.9b03774
57. Hajfathalian, M., et al., A Wulff in a cage: the confinement of substrate-based structures in plasmonic nanoshells, nanocages, and nanoframes using galvanic replacement. ACS nano, 2016. **10**(6): p. 6354-6362. https://doi.org/10.1021/acsnano.6b02712
58. Liu, W., et al., *Self-Assembly of Heterogeneously Shaped Nanoparticles into Plasmonic Metamolecules on DNA Origami.* Chemistry–A European Journal, 2017. **23**(57): p. 14177-14181. https://**doi**.org/10.1002/chem.201703927
59. Godínez-Salomón, F., et al., Metallic Two-Dimensional Nanoframes: Unsupported Hierarchical Nickel–Platinum Alloy Nanoarchitectures with Enhanced Electrochemical Oxygen Reduction Activity and Stability. ACS applied materials & interfaces, 2017. **9**(22): p. 18660-18674. https://doi.org/10.1021/acsami.7b00043
60. Godínez-Salomón, F., et al., Self-Supported Hydrous Iridium–Nickel Oxide Two-Dimensional Nanoframes for High Activity Oxygen Evolution Electrocatalysts. ACS Catalysis, 2018. **8**(11): p. 10498-10520. https://doi.org/10.1021/acscatal.8b02171
61. Zhao, M., et al., Ruthenium nanoframes in the face-centered cubic phase: facile synthesis and their enhanced catalytic performance. ACS nano, 2019. **13**(6): p. 7241-7251. https://**doi**.org/10.1021/acsnano.9b02890
62. Wang, Y., et al., Composition-Dependent Oxygen Reduction Reaction Activity of Pt-Surfaced PtNi Dodecahedral Nanoframes. ACS Applied Energy Materials, 2020. **3**(1): p. 768-776. https://doi.org/10.1021/acsaem.9b01930
63. Bai, X., et al., *Tunable Hollow Pt@Ru Dodecahedra via Galvanic Replacement for Efficient Methanol Oxidation.* ACS Applied Materials & Interfaces, 2020. **12**(20): p. 23046-23050. https://doi.org/10.1021/acsami.0c06460
64. Nosheen, F., et al., *Noble metal based alloy nanoframes: syntheses and applications in fuel cells.* Frontiers in Chemistry, 2019. **7**: p. 456. https://**doi**.org/10.3389/fchem.2019.00456
65. EdEdgar González, 2* Jordi Arbiol,3,4 Víctor F. Puntes1,2,4,5†gar González,1,2* Jordi Arbiol,3,4 Víctor F. Puntes1,2,4,5†, *Carving at the Nanoscale: Sequential Galvanic Exchange and Kirkendal Growth at Room Temperature.* science, 2011. **334**: p. 1377**. https://doi.org/**10.1126/science.1212822.
66. Shi, H., et al., *Photocatalytic template synthesis of Pt nanocages with enhanced electrocatalytic performance.* ECS Electrochemistry Letters, 2015. **4**(8): p. 38. https://**doi**.org/10.1149/2.0061508eel
67. Zhang, X.-F., et al., Solvothermal synthesis of monodisperse PtCu dodecahedral nanoframes with enhanced catalytic activity and durability for hydrogen evolution reaction. ACS Applied Energy Materials, 2018. **1**(9): p. 5054-5061. https://**doi**.org/10.1021/acsaem.8b01065
68. Huang, X.-Y., et al., L-proline assisted solvothermal preparation of Cu-rich rhombic dodecahedral PtCu nanoframes as advanced electrocatalysts for oxygen reduction and hydrogen evolution reactions. Electrochimica Acta, 2019. **299**: p. 89-97. https://**doi**.org/10.1016/j.electacta.2019.01.002
69. Luo, S., et al., Atomic-Scale Preparation of Octopod Nanoframes with High-Index Facets as Highly Active and Stable Catalysts. Advanced Materials, 2017. **29**(8). https://**doi**.org/10.1002/adma.201601687
70. Li, Y., et al., Ag Nanoframes Deposited on Au Films Generate Optical Cavities for Surface-Enhanced Raman Scattering. ACS Applied Nano Materials, 2020. **3**(6): p. 5116-5122. https://doi.org/10.1021/acsanm.0c00393
71. Godínez-Salomón, F., et al., Metallic Two-Dimensional Nanoframes: Unsupported Hierarchical Nickel–Platinum Alloy Nanoarchitectures with Enhanced Electrochemical Oxygen Reduction Activity and Stability. ACS Applied Materials & Interfaces, 2017. **9**(22): p. 18660-18674. https://doi.org/10.1021/acsami.7b00043
72. Kao, C.-R., et al., Insights into Transformation of Icosahedral PdRu Nanocrystals into Lattice-Expanded Nanoframes with Strain Enhancement in Electrochemical Redox Reactions. Chemistry of Materials, 2022**. https://doi.org/**10.1021/acs.chemmater.1c04093
73. Ye, H., et al., *Ru Nanoframes with an fcc Structure and Enhanced Catalytic Properties.* Nano Lett., 2016. **16**: p. 2812. https://doi.org/10.1021/acs.nanolett.6b00607
74. Zhang, L., et al., Low Interface Energies Tune the Electrochemical Reversibility of Tin Oxide Composite Nanoframes as Lithium-Ion Battery Anodes. ACS Applied Materials & Interfaces, 2018. **10**(43): p. 36892-36901. https://doi.org/10.1021/acsami.8b11062
75. Zhang, Y., et al., Mesoporous Silica-Coated Silver Nanoframes as Drug-Delivery Vehicles for Chemo/Starvation/Metal Ion Multimodality Therapy. Langmuir, 2020. **36**(23): p. 6345-6351. https://doi.org/10.1021/acs.langmuir.0c00191
76. Huang, C., et al., *Copper Isolated Sites on N-Doped Carbon Nanoframes for Efficient Oxygen Reduction.* ACS Sustainable Chemistry & Engineering, 2020. **8**(37): p. 14030-14038. https://doi.org/10.1021/acssuschemeng.0c04094

77. Wang, Z., et al., The controllable growth of PtCuRh rhombic dodecahedral nanoframes as efficient catalysts for alcohol electrochemical oxidation. Journal of Materials Chemistry A, 2019. **7**(31): p. 18619-18625. https://doi.org/10.1039/x0xx00000x.
78. Ji, L., et al., *CoP Nanoframes as Bifunctional Electrocatalysts for Efficient Overall Water Splitting*. ACS Catalysis, 2020. **10**(1): p. 412-419. https://**doi.**org/10.1021/acscatal.9b03623
79. Lian, Y., et al., Carved nanoframes of cobalt–iron bimetal phosphide as a bifunctional electrocatalyst for efficient overall water splitting. Chemical science, 2019. **10**(2): p. 464-474. https://doi.org/10.1039/C8SC03877E
80. Ji, L., et al., *Heterointerface Engineering of Ni2P–Co2P Nanoframes for Efficient Water Splitting*. Chemistry of Materials, 2021. **33**(23): p. 9165-9173. https://**doi**.org/10.1021/acs.chemmater.1c02609
81. Wang, A.J., et al., Bimetallic Alloyed PtCu Nanocubic Frames with Three-Dimensional Molecular Accessible Surfaces for Boosting Oxygen Reduction and Glycerol Oxidation Reactions. ChemCatChem, 2018. **10**(15): p. 3319-3326. https://doi.org/10.1002/cctc.201800188
82. Chen, M., et al., Platinum nanoworms self-assemble on β-cyclodextrin polymer inclusion complexes functionalized reduced graphene oxide as enhanced catalyst for direct methanol fuel cells. Journal of Power Sources, 2014. **265**: p. 110-117. https://**doi**.org/10.1016/j.jpowsour.2014.04.031
83. Wang, L., et al., Near-IR-Absorbing Gold Nanoframes with Enhanced Physiological Stability and Improved Biocompatibility for In Vivo Biomedical Applications. ACS Applied Materials & Interfaces, 2017. **9**(4): p. 3873-3884. https://doi.org/10.1021/acsami.6b12591
84. Liu, S., et al., NIR II Light-Response Au Nanoframes: Amplification of a Pressure-and Temperature-Sensing Strategy for Portable Detection and Photothermal Therapy of Cancer Cells. Analytical Chemistry, 2021. **93**(42): p. 14307-14316. https://doi.org/10.1021/acs.analchem.1c03486
85. Hashemi, P., et al., Well-orientation strategy for direct immobilization of antibodies: development of the immunosensor using the boronic acid-modified magnetic graphene nanoribbons for ultrasensitive detection of lymphoma cancer cells. Analytical Chemistry, 2020. **92**(16): p. 11405-11412. https://**doi**.org/10.1021/acs.analchem.0c02357
86. Tang, Y.-H., et al., *Mannosyl electrochemical impedance cytosensor for label-free MDA-MB-231 cancer cell detection.* Biosensors and Bioelectronics, 2018. **116**: p. 100-107. https://doi.org/10.1016/j.bios.2018.05.002
87. Baird, Z., et al., *Tumor cell detection by mass spectrometry using signal ion emission reactive release amplification.* Analytical chemistry, 2016. **88**(14): p. 6971-6975. https://**doi**.org/10.1021/acs.analchem.6b02043
88. Zhang, X., et al., Gold nanoparticles labeling with hybridization chain reaction amplification strategy for the sensitive detection of HepG2 cells by inductively coupled plasma mass spectrometry. Biosensors and Bioelectronics, 2016. **86**: p. 736-740. https://doi.org/10.1016/j.bios.2016.07.073
89. Yu, T., et al., *Highly sensitive colorimetric cancer cell detection based on dual signal amplification.* ACS applied materials & interfaces, 2016. **8**(7): p. 4434-4441. https://doi.org/10.1021/acsami.5b12117
90. Shan, B., et al., Near-Infrared II Plasmonic Au@ Au–Ag Dot-in-Cubic Nanoframes for In Vivo Surface-Enhanced Raman Spectroscopic Detection and Photoacoustic Imaging. Advanced Functional Materials, 2021. **31**(29): p. 2103186. https://doi.org/10.1002/adfm.202103186
91. Zhai, J., et al., *Concave octahedral PtCu nanoframes mediated synergetic photothermal and chemodynamic tumor therapy.* Chemical Engineering Journal, 2022. **442**: p. 136172. https://**doi**.org/10.1016/j.cej.2022.136172
92. Ramanathan, S., et al., *Theranostic applications of nanoparticles in neurodegenerative disorders.* International journal of nanomedicine, 2018. **13**: p. 5561. https://doi.org/10.2147/IJN.S149022
93. Karampelas, I.H., et al., *Plasmonic Nanoframes for Photothermal Energy Conversion.* The Journal of Physical Chemistry C, 2016. **120**(13): p. 7256-7264. https://doi.org/10.1021/acs.jpcc.5b12743
94. Vu, X.H., et al., Tunable LSPR of silver/gold bimetallic nanoframes and their SERS activity for methyl red detection. RSC Advances, 2021. **11**(24): p. 14596-14606. https://doi.org/10.1039/D1RA01477C
95. Yan, Y., et al., Concave octopus-like PtCu nanoframe mediated photo-electro Fenton catalysis for fast organic dyestuff elimination. Nanoscale Advances, 2022. **4**(13): p. 2782-2786. https://doi.org/10.1039/D2NA00233G.
96. Su, T.-y., et al., ZIF-derived metal/N-doped porous carbon nanocomposites: efficient catalysts for organic transformations. Catalysis Science & Technology, 2022. https://**doi**.org/10.1039/D1CY02211C
97. Ganjali, F., et al., Functionalized hybrid magnetic catalytic systems on micro-and nanoscale utilized in organic synthesis and degradation of dyes. Nanoscale Advances, 2022. https://doi.org/10.1039/D1NA00818H
98. Hou, X., et al., *Synthesis and characterizations of spinel MnFe2O4 nanorod by seed–hydrothermal route.* Journal of Alloys and Compounds, 2010. **491**(1-2): p. 258-263. https://doi.org/10.1016/j.jallcom.2009.10.029
99. Chen, C.-H., Y.-H. Liang, and W.-D. Zhang, *ZnFe2O4/MWCNTs composite with enhanced photocatalytic activity under visible-light irradiation.* Journal of Alloys and Compounds, 2010. **501**(1): p. 168-172. https://doi.org/10.1016/j.jallcom.2010.04.072

100. Dom, R., et al., *Synthesis of solar active nanocrystalline ferrite, MFe2O4 (M: Ca, Zn, Mg) photocatalyst by microwave irradiation.* Solid State Communications, 2011. **151**(6): p. 470-473. https://**doi**.org/10.1016/j.ssc.2010.12.034
101. Valero-Luna, C., S. Palomares-Sanchéz, and F. Ruíz, *Catalytic activity of the barium hexaferrite with H2O2/visible light irradiation for degradation of Methylene Blue.* Catalysis Today, 2016. **266**: p. 110-119. https://**doi**.org/10.1016/j.cattod.2015.08.049
102. Du, Y., et al., Trace Amounts of Co3O4 Nano-Particles Modified TiO2 Nanorod Arrays for Boosted Photoelectrocatalytic Removal of Organic Pollutants in Water. Nanomaterials, 2021. **11**(1): p. 214. https://**doi**.org/10.3390/nano11010214
103. a, Y.K., et al., Stepwise synthesis of polyhedral AuAgPd nanoframes plasmon-enhanced catalytic reduction of 4-nitrophenol material letters, 2022. **325**: p. 132808. https://**doi**.org/10.1016/j.matlet.2022.132808
104. a, Y.K., et al., Polyvinyl Alcohol/Silver nanoparticles film prepared via pulsed laser ablation: An eco-friendly nano-catalyst for 4-nitrophenol degradation. Journal of Molecular Structure, 2020. **1212**: p. 128125. https://**doi**.org/10.1016/j.molstruc.2020.128125
105. Zhao, X., et al., *Bimetallic PdAu Nanoframes for Electrochemical H2O2 Production in Acids.* ACS Materials Letters, 2021. **3**(7): p. 996-1002. https://**doi**.org/10.1021/acsmaterialslett.1c00263
106. Bai, J., et al., ZnO/CoO and ZnCo2O4 Hierarchical Bipyramid Nanoframes: Morphology Control, Formation Mechanism, and Their Lithium Storage Properties. ACS Applied Materials & Interfaces, 2015. **7**(41): p. 22848-22857. https://doi.org/10.1021/acsami.5b05303
107. Fang, Y., et al., *Synthesis of CuS@ CoS2 double-shelled nanoboxes with enhanced sodium storage properties.* Angewandte Chemie, 2019. **131**(23): p. 7821-7825. https://**doi**.org/10.1002/anie.201902583
108. Fang, Y., et al., *Synthesis of copper-substituted CoS2@ CuxS double-shelled nanoboxes by sequential ion exchange for efficient sodium storage.* Angewandte Chemie International Edition, 2020. **59**(7): p. 2644-2648. https://**doi**.org/10.1002/anie.201912924
109. Zhang, L., et al., *Synthesizing Cu-doped CoSe2 nanoframe cubics for Na-ion batteries electrodes.* Colloids and Surfaces A: Physicochemical and Engineering Aspects, 2021. **628**: p. 127379. https://**doi**.org/10.1016/j.colsurfa.2021.127379
110. Chen, L., et al., *Interlayer design based on carbon materials for lithium–sulfur batteries: a review.* Journal of Materials Chemistry A, 2020. **8**(21): p. 10709-10735. https://doi.org/10.1039/x0xx00000x
111. Cui, J., et al., *Layered double hydroxides and their derivatives for lithium–sulfur batteries.* Journal of Materials Chemistry A, 2020. **8**(45): p. 23738-23755. https://doi.org/10.1039/d0ta08573a
112. Wang, R., et al., *ZIF-Derived Carbon Nanoframes as a Polysulfide Anchor and Conversion Mediator for High-Performance Lithium–Sulfur Cells.* ACS Applied Materials & Interfaces, 2021. **13**(18): p. 21544-21555. https://**doi**.org/10.1021/acsami.1c04194
113. Ahmed, F., et al., Porous nanoframes of sulfurized NiAl layered double hydroxides and ternary bismuth cerium sulfide for supercapacitor electrodes. Advanced Composites and Hybrid Materials, 2022: p. 1-15. https://**doi**.org/10.1007/s42114-022-00496-1
114. Shinde, N.M., et al., Polycrystalline and mesoporous 3-D Bi2O3 nanostructured negatrodes for high-energy and power-asymmetric supercapacitors: superfast room-temperature direct wet chemical growth. ACS applied materials & interfaces, 2018. **10**(13): p. 11037-11047. https://doi.org/10.1021/acsami.8b00260
115. Kim, S.J., et al., Freestanding binder-free electrodes with nanodisk-needle-like MnCuCo-LTH and Mn1Fe2S2 porous microthorns for high-performance quasi-solid-state supercapacitors. ACS Applied Materials & Interfaces, 2022. **14**(10): p. 12523-12537. https://**doi**.org/10.1021/acsami.1c23945
116. Fu, F., et al., Lamellar hierarchical lignin-derived porous carbon activating the capacitive property of polyaniline for high-performance supercapacitors. Journal of Colloid and Interface Science, 2022. **617**: p. 694-703. https://**doi.**org/10.1016/j.jcis.2022.03.023
117. Yan, M., et al., Construction of a hierarchical NiCo2S4@ PPy core–shell heterostructure nanotube array on Ni foam for a high-performance asymmetric supercapacitor. ACS applied materials & interfaces, 2016. **8**(37): p. 24525-24535. https://**doi**.org/10.1021/acsami.6b05618
118. Zhang, L., et al., *Gold Nanoframes by Nonepitaxial Growth of Au on AgI Nanocrystals for Surface-Enhanced Raman Spectroscopy.* Nano Letters, 2015. **15**(7): p. 4448-4454. https://**doi**.org/10.1021/acs.nanolett.5b01544
119. Go, S., et al., Ring-in-a-Triangle Nanoframes: Integrating with Intra- and Interhotspots for Highly Amplified Near-Field Focusing. Nano Letters, 2022. **22**(4): p. 1734-1740. https://doi.org/10.1021/acs.nanolett.1c04926
120. Chen, S., et al., *High-Performance Pt–Co Nanoframes for Fuel-Cell Electrocatalysis.* Nano Letters, 2020. **20**(3): p. 1974-1979. https://doi.org/10.1021/acs.nanolett.9b05251
121. Kim, D., et al., Quantitative Surface-Enhanced Raman Spectroscopy Analysis through 3D Superlattice Arrays of Au Nanoframes with Attomolar Detection. Analytical Chemistry, 2020. **92**(2): p. 1972-1977. https://doi.org/10.1021/acs.analchem.9b04339

122. Luo, N., et al., High-Sensitive MEMS Hydrogen Sulfide Sensor made from PdRh Bimetal Hollow Nanoframe Decorated Metal Oxides and Sensitization Mechanism Study. ACS Applied Materials & Interfaces, 2020. **12**(50): p. 56203-56215. https://doi.org/10.1021/acsami.0c18369
123. Zhou, Q., S. Yan, and L. Zhang, *Fe-doped MOF-derived N-rich porous carbon nanoframe for H2S cataluminescence sensing.* Luminescence, 2022. https://doi.org/10.1002/bio.4267
124. Bian, Y., et al., *Porous boron nitride: a novel metal-free cataluminescence material for high performance H2S sensing.* Sensors and Actuators B: Chemical, 2021. **332**: p. 129512. https://**doi**.org/10.1016/j.snb.2021.129512
125. Wu, L., et al., Metal-free cataluminescence gas sensor for hydrogen sulfide based on its catalytic oxidation on silicon carbide nanocages. Analytical chemistry, 2017. **89**(24): p. 13666-13672. https://doi.org/10.1021/acs.analchem.7b04566
126. Zhang, Z., et al., *A highly selective chemiluminescent H2S sensor.* Sensors and Actuators B: Chemical, 2004. **102**(1): p. 155-161. https://doi.org/10.1016/j.snb.2004.04.015
127. Pu, S., et al., Recent advances in chemiluminescence and cataluminescence for the detection of volatile sulfur compounds. Applied Spectroscopy Reviews, 2021: p. 1-27. https://doi.org/10.1080/05704928.2021.2016792
128. Hu, Y., et al., Dielectric barrier discharge plasma-assisted fabrication of g-C3N4-Mn3O4 composite for high-performance cataluminescence H2S gas sensor. Sensors and Actuators B: Chemical, 2017. **239**: p. 1177-1184. https://**doi**.org/10.1016/j.snb.2016.08.082
129. Zeng, B., et al., *Fabrication of α-Fe2O3/g-C3N4 composites for cataluminescence sensing of H2S.* Sensors and Actuators B: Chemical, 2015. **211**: p. 370-376. https://**doi**.org/10.1016/j.snb.2015.01.094
130. Liang, S., et al., *Biomimetic inspired porphyrin-based nanoframes for highly efficient photocatalytic CO2 reduction.* Chemical Engineering Journal, 2021. **411**: p. 128414. https://**doi**.org/10.1016/j.cej
131. Chen, X., et al., Metal–organic framework-derived mesoporous carbon nanoframes embedded with atomically dispersed Fe–Nx active sites for efficient bifunctional oxygen and carbon dioxide electroreduction. Applied Catalysis B: Environmental, 2020. **267**: p. 118720. https://**doi**.org/10.1016/j.apcatb.2020.118720
132. Lee, H., et al., *Bimetallic Au/Ag nanoframes as spectator for Co2+ ion.* Journal of industrial and engineering chemistry, 2017. **48**: p. 235-241. https://doi.org/10.1016/j.jiec.2017.01.007
133. Wang, H., et al., *Mesoporous ZrO2 Nanoframes for Biomass Upgrading.* ACS Applied Materials & Interfaces, 2017. **9**(32): p. 26897-26906. https://doi.org/10.1021/acsami.7b07567
134. Zhang, H., et al., Size-Tunable Yolk–Shell Gold–Silver Nanostructures for Photothermal Treatment of Multidrug-Resistant Bacteria. ACS Applied Nano Materials, 2022. https://doi.org/10.1021/acsanm.2c02141
135. Dreaden, E.C., et al., *The golden age: gold nanoparticles for biomedicine.* Chemical Society Reviews, 2012. **41**(7): p. 2740-2779. https://doi.org/10.1039/c1cs15237h
136. Liu, P., et al., Versatile Phenol-Incorporated Nanoframes for In Situ Antibacterial Activity Based on Oxidative and Physical Damages. Advanced Functional Materials, 2022. **32**(17): p. 2110635. https://doi.org/10.1002/adfm.202110635.
137. Hilal, H., et al., *Three-dimensional nanoframes with dual rims as nanoprobes for biosensing.* Nature communications, 2022. **13**(1): p. 1-10. https://**doi**.org/10.1038/s41467-022-32549-w
138. Liu, X.-L., et al., *Tuning plasmon resonance of gold nanostars for enhancements of nonlinear optical response and Raman scattering.* The Journal of Physical Chemistry C, 2014. **118**(18): p. 9659-9664. dx.**doi.**org/10.1021/jp500638u |
139. Chiu, W.-T., et al., Electrocatalytic activity enhancement of Au NPs-TiO2 electrode via a facile redistribution process towards the non-enzymatic glucose sensors. Sensors and Actuators B: Chemical, 2020. **319**: p. 128279. https://**doi**.org/10.1016/j.snb.2020.128279
140. Madriz, L., et al., Photocatalysis and photoelectrochemical glucose oxidation on Bi2WO6: Conditions for the concomitant H2 production. Renewable Energy, 2020. **152**: p. 974-983. https://**doi**.org/10.1016/j.renene.2020.01.071
141. Yang, Y., et al., Flexible Carbon-Fiber/Semimetal Bi Nanosheet Arrays as Separable and Recyclable Plasmonic Photocatalysts and Photoelectrocatalysts. ACS Applied Materials & Interfaces, 2020. **12**(22): p. 24845-24854. https://doi.org/10.1021/acsami.0c05695
142. Wang, C., et al., *Direct Plasmon-Accelerated Electrochemical Reaction on Gold Nanoparticles.* ACS Nano, 2017. **11**(6): p. 5897-5905. https://doi.org/10.1021/acsnano.7b01637
143. Tian, Y., et al., Alloyed AuPt nanoframes loaded on h-BN nanosheets as an ingenious ultrasensitive near-infrared photoelectrochemical biosensor for accurate monitoring glucose in human tears. Biosensors and Bioelectronics, 2021. **192**: p. 113490. https://**doi**.org/10.1016/j.bios.2021.113490
144. Toi, P.T., et al., *Highly Electrocatalytic, Durable, and Stretchable Nanohybrid Fiber for On-Body Sweat Glucose Detection.* ACS Applied Materials & Interfaces, 2019. **11**(11): p. 10707-10717. https://doi.org/10.1021/acsami.8b20583
145. Koskun, Y., et al., *Highly sensitive glucose sensor based on monodisperse palladium nickel/activated carbon nanocomposites.* Analytica Chimica Acta, 2018. **1010**: p. 37-43. https://**doi**.org/10.1016/j.aca.2018.01.035

146. Wang, L., et al., One-step electrodeposition of AuNi nanodendrite arrays as photoelectrochemical biosensors for glucose and hydrogen peroxide detection. Biosensors and Bioelectronics, 2019. **142**: p. 111577. https://**doi**.org/10.1016/j.bios.2019.111577
147. 1, I.A. and M.A.A., 2, Muhammad Khalid 1,2 and Andrey V. Savkin 3,*, *A Comprehensive Review of Recent Advances inSmart Grids: A Sustainable Future with RenewableEnergy Resources.* energies, 2020. **13**: p. 1-41. https://**doi**.org/10.3390/en13236269
148. Shena, Q., et al., Construction of CdSe polymorphic junctions with coherent interface forenhanced photoelectrocatalytic hydrogen generation. Applied Catalysis B: Environmental, 2021. **282**: p. 119552. https://**doi**.org/10.1016/j.apcatb.2020.119552
149. Yong Li a, b., et al., *A 3D C@TiO2 multishell nanoframe for simultaneous photothermal catalytic hydrogen generation and organic pollutant degradation.* Journal of Colloid and Interface Science, 2022. **609**(535-546). https://**doi.**org/10.1016/j.jcis.2021.11.052
150. Ye, S., et al., Unassisted Photoelectrochemical Cell with Multimediator Modulation for Solar Water Splitting Exceeding 4% Solar-to-Hydrogen Efficiency. Journal of the American Chemical Society, 2021. **143**(32): p. 12499-12508. https://**doi**.org/10.1021/jacs.1c00802
151. Domen*, Q.W.a.K., Particulate Photocatalysts for Light-Driven Water Splitting: Mechanisms, Challenges, and Design Strategies. American Chemical Society, 2020. **120(2)**: p. 919-985. https://doi.org/10.1021/acs.chemrev.9b00201
152. Tong Chen, L.L., Cheng Hu, Hongwei Huang *, *Recent advances on Bi2WO6-based photocatalysts for environmental and energy applications.* Chinese Journal of Catalysis, 2021. **42**: p. 1413-1438. https://doi.org/10.1016/S1872-2067(20)63769-X
153. Junmin Huang, J.C., Wangxi Liu, Jingwen Zhang, Junying Chen *, Yingwei Li #, *Copper-doped zinc sulfide nanoframes with three-dimensional photocatalytic surfaces for enhanced solar driven H2 production.* chinese journal of catalysis, 2022. **43**: p. 782-792. https://**doi**.org/10.1016/S1872-2067(21)63864-0